Icarus 249 (2015) 74–92

Contents lists available at ScienceDirect

Icarus

journal homepage: www.elsevier.com/locate/icarus

ChemCam passive reflectance spectroscopy of surface materials at the Curiosity landing site, Mars

Jeffrey R. Johnson [a,*], J.F. Bell III [b], S. Bender [c], D. Blaney [d], E. Cloutis [e], L. DeFlores [d], B. Ehlmann [f], O. Gasnault [g], B. Gondet [h], K. Kinch [i], M. Lemmon [j], S. Le Mouélic [k], S. Maurice [g], M. Rice [f], R.C. Wiens [l], MSL Science Team

[a] Johns Hopkins University Applied Physics Laboratory, Laurel, MD 20723-6005, United States
[b] Arizona State University, Tempe, AZ 85287-0002, United States
[c] Planetary Science Institute, Tucson, AZ 85719, United States
[d] Jet Propulsion Laboratory, Pasadena, CA 91109, United States
[e] University of Winnipeg, Winnipeg, Manitoba, MB R3B 2E9, Canada
[f] California Institute of Technology, Pasadena, CA 91125, United States
[g] Université de Toulouse, CNRS, Institut de Recherche en Astrophysique et Planetologie, Toulouse, France
[h] Institut d'Astrophysique Spatiale, Batîment 12, 91405 Orsay Campus, France
[i] University of Copenhagen, Niels Bohr Institute, Copenhagen, Denmark
[j] Texas A&M University, College Station, TX 77842-3018, United States
[k] Université de Nantes, Laboratoire de Planétologie et Géodynamique, Nantes, France
[l] Los Alamos National Laboratory, Los Alamos, NM 87545, United States

ARTICLE INFO

Article history:
Received 8 October 2013
Revised 5 February 2014
Accepted 23 February 2014
Available online 13 March 2014

Keywords:
Mars
Mars, surface
Spectroscopy

ABSTRACT

The spectrometers on the Mars Science Laboratory (MSL) ChemCam instrument were used in passive mode to record visible/near-infrared (400–840 nm) radiance from the martian surface. Using the onboard ChemCam calibration targets' housing as a reflectance standard, we developed methods to collect, calibrate, and reduce radiance observations to relative reflectance. Such measurements accurately reproduce the known reflectance spectra of other calibration targets on the rover, and represent the highest spatial resolution (0.65 mrad) and spectral sampling (<1 nm) visible/near-infrared reflectance spectra from a landed platform on Mars. Relative reflectance spectra of surface rocks and soils match those from orbital observations and multispectral data from the MSL Mastcam camera. Preliminary analyses of the band depths, spectral slopes, and reflectance ratios of the more than 2000 spectra taken during the first year of MSL operations demonstrate at least six spectral classes of materials distinguished by variations in ferrous and ferric components. Initial comparisons of ChemCam spectra to laboratory spectra of minerals and Mars analog materials demonstrate similarities with palagonitic soils and indications of orthopyroxene in some dark rocks. Magnesium-rich "raised ridges" tend to exhibit distinct near-infrared slopes. The ferric absorption downturn typically found for martian materials at <600 nm is greatly subdued in brushed rocks and drill tailings, consistent with their more ferrous nature. Calcium-sulfate veins exhibit the highest relative reflectances observed, but are still relatively red owing to the effects of residual dust. Such dust is overall less prominent on rocks sampled within the "blast zone" immediately surrounding the landing site. These samples were likely affected by the landing thrusters, which partially removed the ubiquitous dust coatings. Increased dust coatings on the calibration targets during the first year of the mission were documented by the ChemCam passive measurements as well. Ongoing efforts to model and correct for this dust component should improve calibration of the relative reflectance spectra. This will be useful as additional measurements are acquired during the rover's future examinations of hematite-, sulfate-, and phyllosilicate-bearing materials near the base of Mt. Sharp that are spectrally active in the 400–840 nm region.

* Corresponding author.
E-mail address: Jeffrey.R.Johnson@jhuapl.edu (J.R. Johnson).

http://dx.doi.org/10.1016/j.icarus.2014.02.028
0019-1035/

1. Introduction

1.1. Overview

The Laser-Induced Breakdown Spectrometer (LIBS) portion of the Chemistry and Camera (ChemCam) instrument on the Mars Science Laboratory (MSL) rover Curiosity uses three dispersive spectrometers to cover the ultraviolet (UV; 240–342 nm), blue–violet (VIO; 382–469 nm) and visible/near-infrared (VNIR; 474–906 nm) spectral regions at high spectral (<1 nm) and spatial (0.65 mrad) resolution. In active LIBS mode, light emitted from a laser-generated plasma is dispersed onto these spectrometers and used to detect elemental emission lines (Wiens et al., 2012; Maurice et al., 2012). During instrument development it was understood that the ChemCam spectrometers exhibited sufficient sensitivity to allow collection of potentially useful surface spectral reflectance in passive mode (i.e., without using the laser). However, the spectrometers were not radiometrically calibrated to a specific accuracy requirement for this purpose. Nonetheless, it was recognized that radiance observations of well-characterized Mastcam and ChemCam calibration targets on the Curiosity rover provided the opportunity to transform radiance spectra of surface targets to relative reflectance and thereby test the passive spectral capability of ChemCam on Mars. Here we present a method to calibrate passive radiance measurements to relative reflectance, and we discuss preliminary spectra (400–840 nm) of rocks, dust, soils, and calibration target surfaces observed during the first 360 sols of the Curiosity mission (August 5, 2012–August 11, 2013), comprising ~2100 observations on ~260 separate targets.

1.2. Background

Visible/near-infrared (400–1000 nm) spectra have been used for decades as a key means of constraining mineralogy and crystallinity of iron-bearing minerals on Mars and in the laboratory (e.g., Singer et al., 1979; Bell et al., 2000, 2008). Ferric iron absorptions cause strong, positive slopes from the blue to red wavelengths, with relative reflectance maxima typically near 750 nm. On Mars this absorption edge is steeper in spectra of brighter (often more dust-coated) regions than darker regions. In practice, spectral ratios of red/blue wavelengths provide first-order information on the relative level of oxidation of surface materials and/or degree of dust coatings (e.g., Johnson and Grundy, 2001; Johnson et al., 2003). For example, relatively dust-free "gray" rocks observed by Mars Pathfinder and the Mars Exploration Rovers exhibited lower red/blue color ratios than more dust-coated surfaces (McSween et al., 1999; Bell et al., 2004a,b; Farrand et al., 2006, 2007, 2008a,b). Relatively weak absorptions near 535 nm and in the 800–1000 nm region are consistent with the presence of crystalline ferric oxides such as hematite (Bell et al., 2004a,b). The curvature of the spectrum near 600 nm is related to the strength of the short wavelength ferric oxide absorption edge, and can be indicative of the presence of other Fe^{3+}-bearing phases (e.g., goethite), which have an additional weak ~660 nm absorption. Many hydrated iron-bearing sulfate and ferric oxide minerals (e.g., hematite) have prominent 800–860 nm absorptions and relatively short wavelength reflectance maxima (Johnson et al., 2007; Lane et al., 2008). The reflectance decrease towards the near-infrared is also attributable to the presence of ferrous iron absorption bands associated with mafic silicate minerals such as pyroxenes and olivine (e.g., Roush et al., 1993).

2. Methods

2.1. Passive spectra: acquisition

Each ChemCam spectrometer records 2048 spectral channels, thus providing 6144 total channels per observation (Wiens et al., 2012; Maurice et al., 2012). The spectral resolution varies with each spectrometer: 0.15 nm (UV), 0.20 nm (VIO), and 0.61 nm (VNIR). LIBS observations acquired by ChemCam included a companion 3 ms exposure "dark" passive measurement (obtained without use of the laser). This measurement was most often acquired after laser shots at a particular location, although certain experiments (detailed below) included dark measurements prior to and after laser shots to study the effects of dust removal caused by the laser (Graff et al., 2011; Meslin et al., 2013). Because it was initially considered unlikely that such short exposure times would provide sufficient signal for analyses of relative reflectance (particularly in the UV and VIO spectrometers), we developed dedicated passive observations to use longer exposure times for reach of the three spectrometers (5000 ms for UV, 400 ms for VIO, and 30 ms for VNIR) to maximize signal. Such observations were typically acquired at the location of the last laser shots in a ChemCam LIBS raster of points, or at specified locations on the calibration targets (Section 2.3). These exposure times (in addition to the standard 3 ms exposure obtained for the dark measurements) were taken in sequence and consistently used for both targets of interest and the calibration targets to facilitate comparisons by minimizing differences in instrument dark current. Multiple spectra at each exposure time were acquired at a single location and averaged to improve signal-to-noise ratio (SNR): typically 5 spectra for the 3 ms and 30 ms exposures, and 30 spectra for the 400 ms and 5000 ms exposures. Some spurious pixel behavior was observed in the spectrometers, particularly with the longer integration times used in the passive spectra data acquisitions. But this dominantly resulted from "popcorn noise" and detector response non-uniformity. The UV spectrometer exhibited two "hot pixels" but those were not severe. The amount of pixel-wavelength shift resulting from spectral smile is a fraction of a pixel, i.e., small compared to the rate of change of the smile across the array. Because the spectral features of interest here are much broader in wavelength, the impact of this on the data analysis is minimal.

2.2. Passive spectra: radiance calibration

For a given passive observation, data numbers (DN, or counts) obtained from each of the three spectrometers were first corrected for inherent background noise by subtracting the average DN values from regions that exhibited near-zero radiometric response in the UV (channels 4385–4395), VIO (channels 2237–2241), and VNIR (channels 1905–1920) spectrometers. The resultant values were then converted to photons by multiplication of the ChemCam instrument response function (units of photons/DN) (Wiens et al., 2012). The distance (d) to the target was used in combination with spectrometer angular field-of-view (FOV) (0.65 mrad) to calculate the associated area (A) on the target:

$$A = \pi(\mathrm{FOV} * d/2)^2$$

The solid angle (SA) subtended by the telescope aperture (a = 108.4 mm) is

$$SA = \pi * \sin\left(\arctan((a/2)/d)\right)^2$$

Radiance values (RAD, photons/s/cm^2/sr/nm) were then calculated by dividing the photons (P) by the integration time (t), spectral bin width (w), and the area and solid angle of the measurement:

$$RAD = P/t/A/SA/w$$

These values were converted to more standard units of W/m^2/sr/μm. Estimates for the VNIR, VIO, and UV 3-sigma absolute calibration uncertainty upon landing are ~6%, ~8%, and ~20%, respectively.

2.3. Calibration target analyses

2.3.1. Overview

The ChemCam calibration targets (CCCTs) were constructed to provide onboard standards to assist interpretations of emission spectra obtained from ChemCam active measurements. As described in Fabre et al. (2011), Vaniman et al. (2012) and Wiens et al. (2012), the CCCT comprises ten numbered calibration standards (Fig. 1): Four glasses of igneous composition (#1–#4), a graphite (target #5), four granular ceramic targets (#6–#9), and a titanium metal plate (#10) used for wavelength calibration of LIBS data. The ceramic targets are composed of sintered powders of basalt, anhydrite, and phyllosilicate materials (kaolinite and smectite) with variable sulfate (anhydrite) contents. The ceramic targets also contain a large amorphous component (33–71%) but some residual ferric oxide minerals (hematite) are present. Targets #1–#9 were manufactured as 22 mm diameter discs housed in a target holder coated with a high reflectance, zinc stearate-based coating. The visible portions of the targets in the assembly are 18 mm diameter holes. Fig. 2 shows laboratory visible/near-infrared reflectance spectra of these targets, including that of the target holder coating, referred to as Target #11 (located between Targets #4, #5, and #9). This material has high reflectance (~95%) and is nearly spectrally flat at wavelengths >400 nm, which enables its use as an effective calibration standard.

The Mastcam calibration target provides surfaces with 20%, 40%, 60% reflectance rings ("black", "gray", and "white", respectively) and pigmented color chips used to help validate the pre-flight calibration of the Mastcam imaging system (Fig. 1). These targets are also well-characterized in the visible/near-infrared, with heritage from the Mars Exploration Rover (MER) missions (Bell et al., 2003). Observations of the calibration target (caltarget) are typically used to calibrate Mastcam multispectral images (Bell et al., 2013) and track deposition of airfall-deposited dust on the rover deck (Kinch et al., 2013). The Mastcam caltarget also includes six small "sweep magnets" mounted beneath the white and gray rings and beneath each of the four color chips (cf. Madsen et al., 2009). The magnets are 5 mm tall hollow cylinders with an outer diameter of 9 mm and an inner diameter of 4 mm, designed to produce an upward-directed magnetic field gradient just above the center of the magnet. This causes an upward force on airborne magnetic particles (dust grains), resulting in reduced dust deposition on surfaces above the center of the magnet (cf. Goetz et al., 2005, 2008). As such, the central regions of the magnets were expected to represent minimally dust-contaminated surfaces and thus potentially robust calibration standards. (For comparison, the 37.9° tilt of the CCCT on the rover deck mitigated dust deposition somewhat, as discussed further in Section 2.3.2).

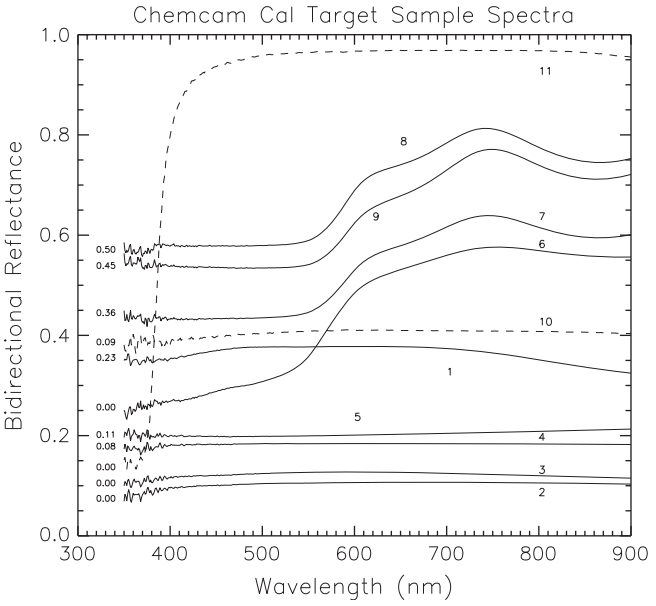

Fig. 2. Bidirectional reflectance spectra of CCCT materials (after Wiens et al., 2012). Targets #1–9 were measured in the laboratory (using an Analytical Spectral Devices spectrometer) at 30° incidence angle and 9.5° emission angle (typical viewing geometry for ChemCam observations of the CCCT). Targets #10–11 saturated the signal in that geometry, and were instead measured at 60° incidence and 9.5° emission. Numbered spectra correspond to targets numbered in Fig. 1. Spectra offset for clarity by amount shown to left of each.

Fig. 1. Portion of Mastcam image acquired during pre-flight rover testing showing Mastcam and ChemCam calibration target (CCCT) locations on rover deck. CCCT targets numbered, including target holder (Target #11) used for calibration of passive spectra.

2.3.2. Dust coating effects

Because the ChemCam team designed observation sequences during pre-flight testing to target the CCCT, passive observations of the Target #11 region were more straightforward to acquire early in the mission than observations of the Mastcam target, which was at the ChemCam close focus distance limit (~1.17 m). Fig. 3 shows representative remote micro-imager (RMI) images of the Target #11 region from three different sols (cf., Maurice et al., 2012; Wiens et al., 2012; Le Mouélic et al., 2015). Table 1 lists all observations of Target #11 acquired during the first 360 sols, the solar incidence angle corrected for the 37.9° tilt of the CCCT (referred to here as the local incidence angle, inc_L), and preliminary atmospheric opacity values calculated from Mastcam observations at 880 nm using the techniques of Lemmon et al. (2004).

The main goal of acquiring repeated measurements of Target #11 was to provide calibration target data relatively close in time, and at similar times of day, to surface observations to facilitate calibration under similar atmospheric opacity and solar illumination conditions. It was expected that variability in radiance values from Target #11 during the mission would result from differences in: (a) airfall dust deposition and erosion; (b) solar and viewing geometry; and (c) atmospheric opacity. Qualitative changes in the amount of dust on the Target #11 surface are apparent in RMI images (e.g., Fig. 3), suggesting an overall net deposition of dust

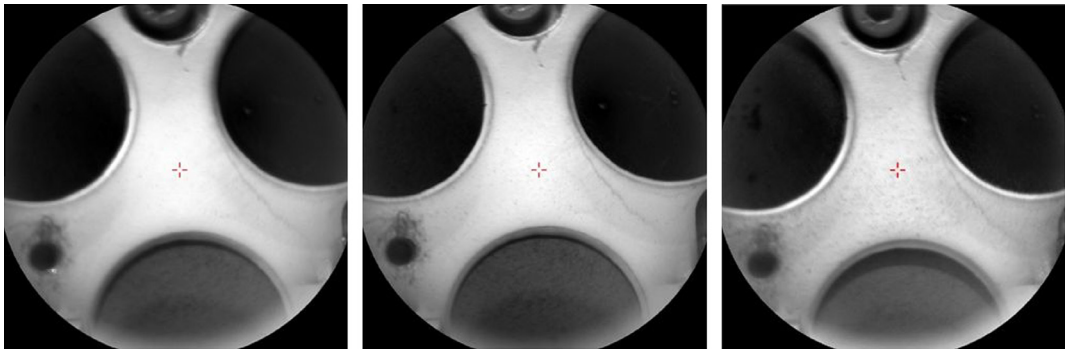

Fig. 3. Remote micro-imager (RMI) images from Sols 34, 76, and 341 of the Target #11 location on the ChemCam calibration target holder (cf. Fig. 1). RMI field of view is ~33 mm in each image. (Image IDs: CR0_400508405EDR_F0040000CCAM01034, CR0_404238394EDR_F0050104CCAM02076 CR0_427761865EDR_F0050104CCAM06339.) Cross represents location from which spectra were acquired. At the 1582 mm distance of Target #11, the sampled region of passive ChemCam spectra is ~1 mm (0.65 mrad).

Table 1
ChemCam observations of calibration Target #11.

Sol	Sequence ID	Exposure times (ms)	LTST	inc_L (°)	τ_{880}[a]
33	3033	3	13:04	43.4	0.69
43	1043	3/30/400/5000	12:21	63.0	0.71
57	3057	30/400/5000	12:33	42.2	0.67
76	2076	3/30/400/5000	12:52	38.1	0.71
87	2087	3/30/400/5000	12:30	44.0	0.61
100	2100	3/30/300[b]/5000	13:11	34.5	1.17
112	1112	3/30/400/5000	12:33	58.6	1.15
135	7135	30/400/5000	13:17	26.5	1.10
148	4148	30/400/5000	12:12	32.6	1.02
153	1153	3/30/400/5000	14:53	33.5	1.06
169	1169	3/30/400/5000	14:57	56.4	1.10
176	4176	3/30/400/5000	12:22	33.2	0.96
183	3183	3/30/400/5000	12:34	34.3	0.92
230	1230	3/30/400/5000	11:40	30.0	0.70
269	1269	3/30/400/5000	12:01	37.4	1.32
281	3281	3/30/400/5000	10:55	46.6	1.02
293	3292	3/30/400/5000	14:28	40.9	0.93
306	3305	3/30/400/5000	12:11	38.0	0.85
318	2318	3/30/400/5000	11:00	41.1	0.87
321	7319	3/30/400/5000	12:02	46.5	0.83
330	3330	3/30/400/5000	11:13	60.7	0.73
341	6339	3/30/400/5000	11:00	67.3	0.70
350	1350	3/30/400/5000	11:56	55.9	0.75

[a] Interpolated from preliminary atmospheric opacity measurements acquired at 880 nm.
[b] Sequencing error resulted in 300 ms instead of 400 ms exposure.

during the mission. Because one of the REMS instrument wind sensors was damaged upon landing, direct wind measurements have uncertainties on wind speeds and direction (Vasavada et al., 2013), minimizing their potential use to investigate wind effects on dust coatings.

To investigate geometric effects, we first compared radiance values at 593 nm (typically the maximum) for Target #11 to Sol number, inc_L, the difference between solar and instrument angle, and phase angle (Fig. 4). Radiance values decrease overall as a function of time, but are also sensitive to illumination and viewing angles. Because a photometric function of the Target #11 material is not available to quantify the amount of specular vs. diffuse scattering, we attempted to correct for the viewing and illumination trends by dividing the radiance values by $\cos(inc_L)$, which we refer to hereafter as *RAD**. The results demonstrate an improvement in removing these observed trends, although a decrease in radiance with time is still evident.

We next compared the *RAD** values to preliminary atmospheric opacity values at 880 nm (τ_{880nm}) from Mastcam observations, shown in Fig. 5. Lower radiance values from Target #11 might be expected at elevated τ_{880nm} values owing to the greater dust load in the optical path to the CCCT. However, typically on Mars increases in τ_{880nm} are prefaced by wind activity and dust lifting, followed by slow fallout of atmospheric dust. If *RAD** values from Target #11 vary with the amount of airfall-deposited dust contamination, one would expect increases in *RAD** before large increases in τ_{880nm} as a result of dust erosion from Target #11. This would be followed by a steady decrease in *RAD** values due to deposition of airfall dust particles. In Fig. 5, *RAD** values increased slightly prior to the Sols 98–100 onset of high τ_{880nm} values, and then decreased afterwards until Sol 153. However, subsequent *RAD** values increased until leveling between Sols 183 and 230, while τ_{880nm} values continued to decrease. Similarly the increase in τ_{880nm} values after Sol 240 was accompanied by a decrease in *RAD** until Sol 293, followed by minor increases until Sol 341, all while τ_{880nm} values steadily decreased.

Rover driving may also alter dust content on the calibration targets, although the correlation between drive sols and *RAD** values is poor (e.g., *RAD** values vary while the rover was stationary between Sols 60 and 99, and between Sols 161 and 271). Rover arm brushing activities (while the rover was parked) occurred on Sols 150, 169, and 291, and rover drilling activities on Sols 183 and 279. However, there is no consistent correlation between changes in *RAD** values and these activities. Furthermore, it is unlikely that vibrations related to brushing or drilling activities would be transmitted through the rover body sufficiently to affect dust on the CCCT surface (L. Jandura, personal communication, 2013).

We next investigated the spectral reddening effects of dust deposition on Target #11 in detail by dividing all *RAD** spectra of Target #11 (3 ms exposure times) by the first available measurement acquired on Sol 33 (cf. Table 1). Fig. 6 shows the resulting ratio spectra, all normalized to 1.0 at 700 nm to facilitate comparison to Sol 33 spectra (represented by a flat line at 1.0). Although variations in the spectra occur among sols, an overall reddening develops during the course of the mission that can be attributed to dust deposition. Sol 43 appears to be more affected by dust than Sols 76 or 87, but based on the spectral slopes in the 400–600 nm region Target #11 did not become less contaminated than it was on Sol 76 after Sol 100.

2.4. Relative reflectance spectra

Ideally, observations of the Target #11 surface would have been acquired close in time to a given surface observation in order to minimize changes in solar illumination and atmospheric opacity variations. However, owing to the resource limitations and appropriately lower priority of these measurements, comparatively few observations were acquired (Table 1). Given the results of Fig. 6, we preferred to eliminate uncertainties regarding variations in

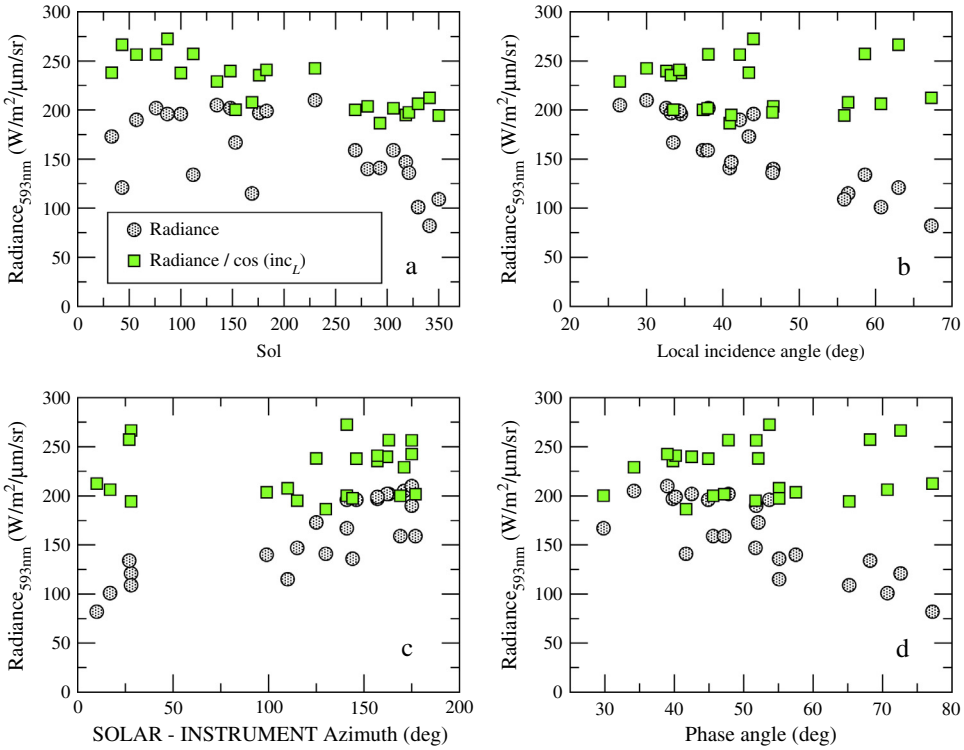

Fig. 4. Radiance values (at 593 nm) of Target #11 observations as a function of (a) Sol number; (b) local incidence angle (inc_L); (c) difference between Sun azimuth and instrument azimuth; and (d) phase angle. Overall trends are mitigated somewhat via division by cos(inc_L).

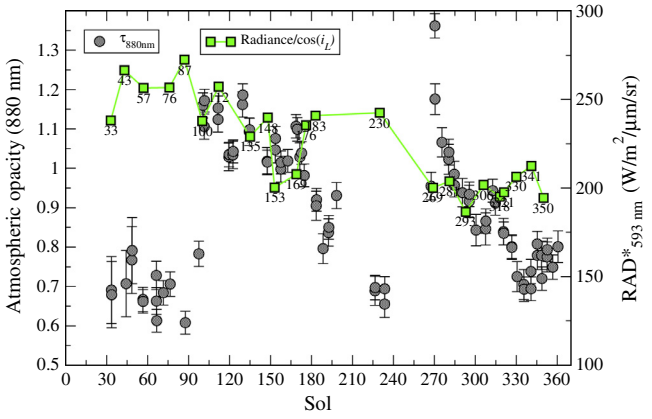

Fig. 5. Preliminary atmospheric opacity values (880 nm) as a function of Sol number, compared to radiance values (at 593 nm) of Target #11 observations (labeled by Sol number).

dust contamination. Therefore, we elected to use Target #11 observations from Sol 76 as the main standards for comparison to all ChemCam passive spectra presented here. This Sol 76 sequence acquired spectra at all four relevant exposure times (3, 30, 400, 5000 ms), was obtained under intermediate values of τ_{880nm} (~0.71) and inc_L (~38°), and appeared to be least contaminated with dust relative to the Sol 33 observation. Residual uncertainties will result from variations in atmospheric opacity and lighting geometry between Sol 76 and a particular observation. But we expect these effects to either raise or lower overall radiance values or induce small changes in spectral slope, both of which are preferable to large changes in spectral features that would otherwise result from using heavily dust-coated calibration standards. In Section 6.2.3 we describe future possible refinements to this technique that are beyond the scope of the present work, including incorporation of a photometric function of the Target #11 material and a dust-correction method similar to that used for Mastcam and MER Pancam observations (Kinch et al., 2007, 2013; Johnson et al., 2006).

Because the Target #11 material has near-zero reflectance <400 nm, the UV spectrometer data cannot be calibrated using the methods described here. Alternative methods that could be pursued are described further in Section 6.2.2. In addition, VNIR spectrometer responsivity past ~840 nm and VIO spectrometer responsivity below ~400 nm are relatively low. As such, for the purposes of this paper we restrict analyses to 400–840 nm. For dedicated passive observations (comprising three spectra with 30, 400, and 5000 ms exposure times), a combined spectrum was obtained by extracting the relevant data from each spectrometer region. We also note that the temperature of the ChemCam spectrometers influences the VIO (and UV) signal-to-noise ratio. Typical operating temperatures for ChemCam (determined by the "BU_CCD_UV_A" onboard sensor) range from −10 °C to 5 °C, but can exceed 10 °C for late-afternoon observations. At such temperatures, increases in noise can dominate the VIO spectrum and noticeably affect the VNIR spectrum at shorter wavelengths.

For all spectra acquired of rocks, soils, and other calibration targets, we divided radiance spectra acquired at a given exposure time by the corresponding Sol 76 *RAD** spectrum, and then multiplied the result by the laboratory bidirectional reflectance spectrum of Target #11 (Fig. 2) to produce a relative reflectance (*R*) spectrum. In general, this method follows the typical procedure established for terrestrial field spectroscopy (e.g., Johnson et al., 2001; Milton et al., 2009), in which a scene spectrum is divided by a calibration target spectrum and then multiplied by the calibration target laboratory spectrum to generate an estimate of *R*. Given the 6–8% relative uncertainty of the ChemCam passive radiance spectra, it is likely that the overall precision of relative

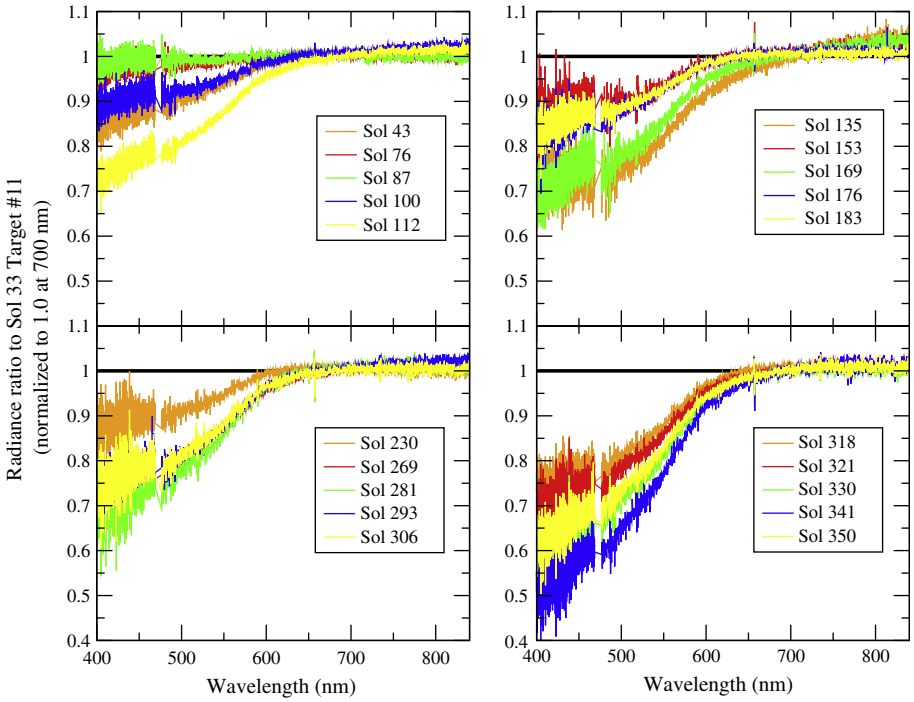

Fig. 6. *RAD** spectra of all Target #11 observations (acquired at 3 ms exposure time) divided by Sol 33 measurement (cf. Table 1), normalized to 1.0 at 700 nm. Horizontal line at ratio value 1.0 corresponds to no change from Sol 33. Increased reddening with time is caused by dust deposition on the calibration target. (For the interpretation of the references to color in this figure legend, the reader is referred to the web version of this article.)

reflectance spectra is 10–20%. Comparisons to Mastcam spectra (described in Section 4.2) are consistent with this estimate.

3. Data sets

3.1. Calibration targets

In addition to the Target #11 CCCT observations (Table 1), dedicated observations at 30, 400, and 5000 ms exposures were acquired of the other CCCT materials during Sols 30–33 (Table 2). In addition, later in the mission an observation sequence was designed to acquire passive spectra of Target #11, Target #6 (“Kaolinite”), and Target #5 (“Graphite”) as part of a “triad” campaign to provide spectra of three different reflectance materials to test dust-correction models, as described in Section 6 (Table 2).

RMI images were acquired during pre-flight testing of the Mastcam calibration target’s white ring and green color chip. These images were used to establish pointing of passive spectra of these two targets on Mars, which was first attempted unsuccessfully on Sol 45, refined on Sol 87, and repeated three more times. Subsequently, a 5-location passive raster observation was designed to begin at the center of the sweep magnet under the white ring, extend through magnetic dust, and onto the white ring proper. Fig. 7 shows the location of these targets, along with a set of observations that targeted the black, gray, and white rings as another “triad” sequence designed to provide input to future dust-correction models (Table 3).

Table 2
ChemCam calibration target dedicated passive observations.

Sol	Sequence ID	Target number	Exposure times	Number collects
32	1032	1	30/400/5000	5/30/30
33	2033	2	30/400/5000	5/30/30
33	2033	3	30/400/5000	5/30/30
33	2033	4	30/400/5000	5/30/30
30	2030	5	30/400/5000	5/10/30
30	2030	6	30/400/5000	5/10/30
32	1032	7	30/400/5000	5/30/30
30	2030	8	30/400/5000	5/10/30
32	1032	9	30/400/5000	5/30/30
30	1030	11 (paint)[a]	30/400/5000	5/10/30
306	3305	5, 6, 11	3/30/400/5000	5/5/30/30
321	7319	5, 6, 11	3/30/400/5000	5/5/30/30
330	3330	5, 6, 11	3/30/400/5000	5/5/30/30
341	6339	5, 6, 11	3/30/400/5000	5/5/30/30
350	1350	5, 6, 11	3/30/400/5000	5/5/30/30

[a] Target pointing incorrect; data not used.

3.2. Surface targets

Dedicated passive spectra (exposure times of 30, 400, and 5000 ms) were acquired of 23 targets (19 rocks, 2 soils, 2 drill tailings), typically at the location of the last LIBS analysis in a raster (grid) or linear array of points (Table 4). As described above, our initial expectations were that the standard 3 ms exposure time used for “dark” measurements (acquired before and/or after LIBS laser shots) would not provide sufficient signal for reflectance measurements. However, as shown in Section 4.2 the 3 ms exposure provided very suitable spectra in the VNIR region and often in the VIO region. As such, we also present results from raster and linear arrays acquired for 209 rock targets (1796 individual reflectance spectra), and 41 soil targets or drill tailings (342 spectra). In some instances “rock” targets included measurements of nearby soil, and some “soil” measurements sampled small pebbles. In addition, about 5% of the rock target points were in shadow, thereby compromising the reflectance spectra (as described in Section 4.4). Furthermore, the 30–150 laser shots used for LIBS measurements at a single location often resulted in partially shadowed holes in soils that measured on average about half the diameter of the ChemCam spectrometers’ field of view. As such, soil relative reflectance spectra values are somewhat lower than the undisturbed surface. This effect was investigated in detail via

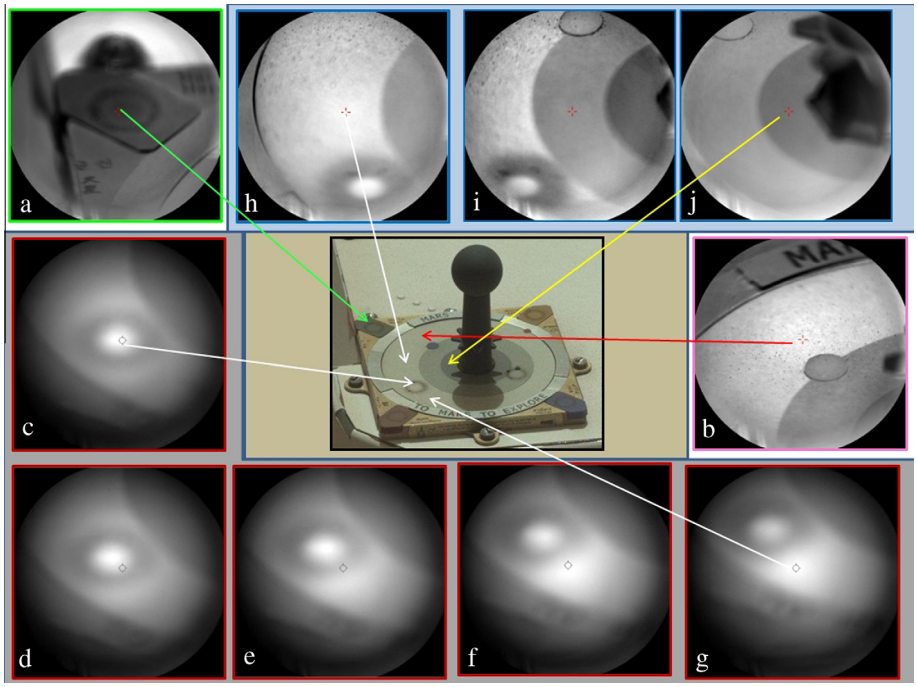

Fig. 7. Mastcam image of Mastcam calibration target (*center*) and example RMI images associated with passive spectra sequences that targeted portions of the calibration target: (a) green color chip, Sol 87, CR0_405213270EDR_F0050104CCAM01087; (b) white ring, Sol 87, CR0_405212936EDR_F0050104CCAM01087; (c) center of sweep magnet under white ring, Sol 193, CR0_414625901EDR_F0060000CCAM03193; (d–g) 4 locations extending away from magnet area, Sol 193: CR0_414626269EDR_F0060000CCAM03193; CR0_414626557 EDR_F0060000CCAM03193; CR0_414626845EDR _F0060000CCAM03193; CR0_414627133EDR _F0060000CCAM03193, respectively (h–j) white, gray, and black rings, Sol 321: CR0_425992118EDR_F0060804CCAM08319; CR0_425991827EDR_F0060804CCAM08319; CR0_425991510EDR_F0060804CCAM08319, respectively. Mastcam calibration target is 8 cm on a side (portion of image 0013ML0002010000E1_DXXX) (cf. Tables 2 and 3). (For interpretation of the references to color in this figure legend, the reader is referred to the web version of this article.)

Table 3
ChemCam observations of Mastcam calibration target regions.

Sol	Sequence ID	Mastcam target	Exposure times	Number collects
45[a]	2045	Green chip	30/400/5000	5/30/30
87	1087	Green chip	30/400/5000	5/30/30
148	3148	Green chip	30/400/5000	5/30/30
273	7271	Green chip	30/400/5000	5/30/30
355	3353	Green chip	30/400/5000	5/30/30
45[a]	2045	White ring	30/400/5000	5/30/30
87	1087	White ring	3/30/400/5000	5/5/30/30
148	3148	White ring	3/30/400/5000	5/5/30/30
273	7271	White ring	3/30/400/5000	5/5/30/30
355	3353	White ring	3/30/400/5000	5/5/30/30
169	2169	White magnet *center*	3/30/400/5000	5/5/30/30
193	3193	White magnet raster	3/30/400/5000	5/5/30/30
273	6271	White magnet raster	3/30/400/5000	5/5/30/30
310	3310	White magnet raster	3/30/400/5000	5/5/30/30
350	2350	White magnet raster	3/30/400/5000	5/5/30/30
310	4310	White, gray, black rings	3/30/400/5000	5/5/30/30
321	8319	White, gray, black rings	3/30/400/5000	5/5/30/30
330	4330	White, gray, black rings	3/30/400/5000	5/5/30/30
341	5339	White, gray, black rings	3/30/400/5000	5/5/30/30
350	3350	White, gray, black rings	3/30/400/5000	5/5/30/30

[a] Target pointing incorrect; data not used.

experiments that acquired passive spectra before and after laser shots on both rocks and soils, as discussed in Section 4.3.1.

4. Results

4.1. Calibration targets

ChemCam relative reflectance spectra of the CCCT and Mastcam calibration targets provided important first-order confirmation of the ability of the methods described above to accurately reproduce known reflectance spectra. Fig. 8 shows dedicated ChemCam passive reflectance spectra of the CCCTs acquired on Sols 30–33 (Table 2) calibrated using the Sol 76 Target #11 and divided by their respective $\cos(inc_L)$ values. Comparison to the laboratory spectra (also divided by the 30° incidence angle used during their acquisition) shows excellent agreement. Fig. 9 shows passive spectra of the Mastcam calibration target white ring and green color chip (Table 3) at four times from Sols 87 to 355, compared to laboratory spectra of the same materials (Bell et al., 2003). The

Table 4
ChemCam observations with dedicated passive measurements.

Sol	Sequence ID	Target name	Target type
32	2032	Pekanatui	Rock
32	3032	Taltheilei	Rock
45	1045	JM_1 on Jake_Matijevic	Rock
49	3049	Anton	Soil
57	2057	Rocknest_3	Rock
61	2060	Pearson	Rock
72	4072	Kilian	Rock
104	2104	Acasta	Rock
111	1111	Amagok	Rock
111	2111	Asiak	Rock
114	2114	Jackson_Lake	Rock
114	1114	Patterson_Lake	Rock
117	3117	Jackson_Lake_3	Rock
135	2135	Rapitan	Rock/vein
135	4135	Pachi	Soil
135	6135	Rackla	Rock
176	3176	Nanok	Rock
183	1183	Wernecke2	Brushed rock
183	2183	John_Klein	Drill tailings
184	6184	Nanok_2	Rock (exposed)
281	1281	Cumberland	Drill tailings
293	1292	Cumberland	Brushed rock
337	3337	Ashuanipi	Rock

Sol 87 data reproduce the lab spectra well in spectral shape and relative reflectance, particularly the green color chip. But the effects of dust deposits on both targets become pronounced with time, similar to the dust effects on Target #11 radiance ratios observed in Fig. 6.

4.2. Surface targets

Armed with the knowledge that the ChemCam passive spectra adequately reproduced the laboratory spectra of the onboard calibration targets, we gained confidence that spectra of martian surface targets would be relatively accurate. Additional verification was possible by comparing ChemCam spectra to Mastcam multispectral spectra of the same targets (e.g., Bell et al., 2013), to orbital visible/near-infrared spectra of the Curiosity landing site, and to laboratory spectra of Mars analog materials. Fig. 10 compares ChemCam relative reflectance spectra from the low albedo soil "Anton" observed in a rover track on Sol 49 to preliminary Mastcam spectra of the same soil. The overall shape and relative reflectance levels are quite similar. Also shown in Fig. 10 are laboratory spectra of the Mars analog soil JSC-1, a palagonitic Hawaiian soil, visible detector spectra from the OMEGA instrument on Mars Express for the Curiosity landing site (cf. Bibring et al., 2004; Gondet et al., 2013) and from typical "bright" and "dark" areas (Ody et al., 2012), as well as visible detector spectra from the CRISM instrument on Mars Reconnaissance Orbiter for the Curiosity landing site (Seelos et al., in preparation). The similarity of these spectra provides additional assurance regarding the first-order calibration of the ChemCam (and Mastcam) relative reflectance spectra. The spectral similarity to palagonitic soils is consistent with the results from the CheMin instrument for nearby soils in the Rocknest area that demonstrated similar mineralogy to Hawaiian palagonitic soils (Bish et al., 2013; Blake et al., 2013).

Fig. 11 shows the variety of spectral features obtained from all the dedicated passive spectra listed in Table 4. Although most spectra exhibit a ferric absorption edge shortward of ~600 nm and a broad band centered near 535 nm typical for dusty regions on Mars, the degree of dust contamination (and overall relative reflectance values) varies from relatively low (e.g., Rocknest3, Sol 57) to very dust-covered (e.g., Taltheilei, Sol 32). Light-toned veins interpreted to be Ca-sulfate rich on the basis of LIBS data combined with Mastcam and CheMin analyses (e.g., Nachon et al., submitted for publication, 2014; Grotzinger et al., 2013; Vaniman et al., 2013;

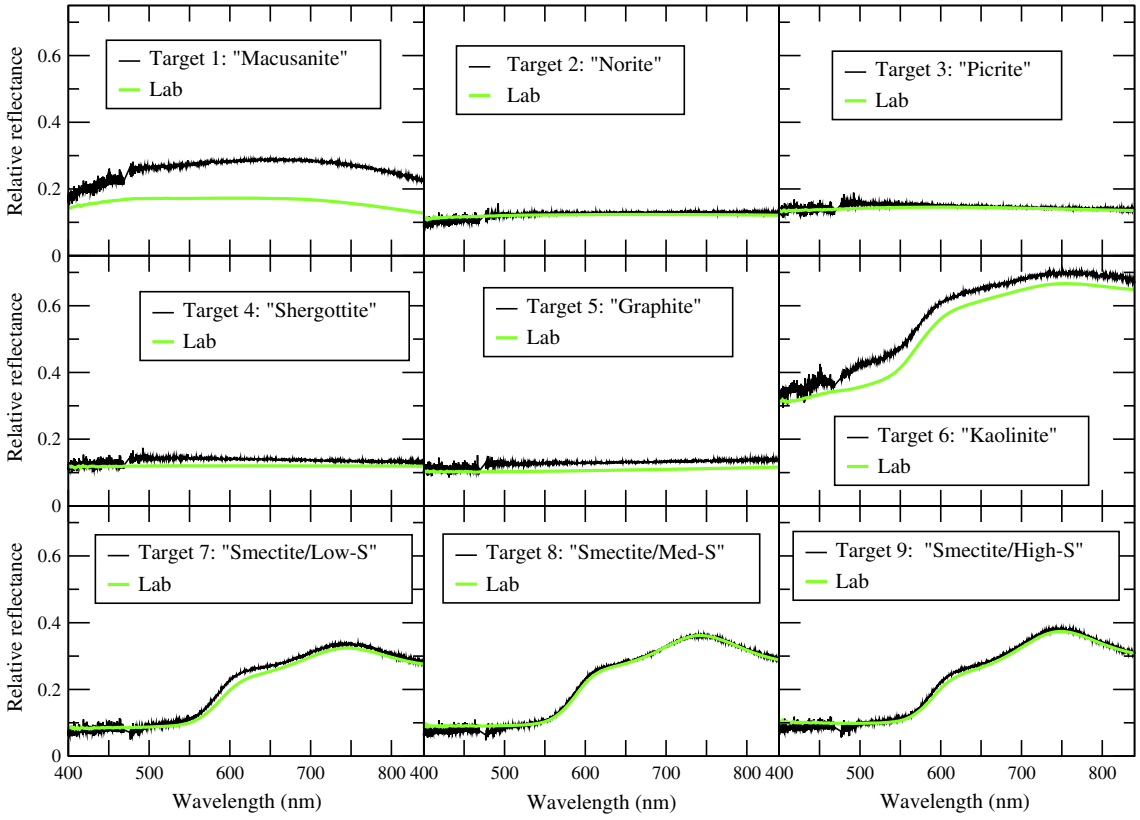

Fig. 8. ChemCam passive reflectance spectra of CCCTs acquired on Sols 30–33 (Table 2) calibrated using Sol 76 Target #11 spectra, compared to laboratory bidirectional reflectance spectra (Fig. 2). ChemCam spectra represent combined 30 ms (VNIR) and 400 ms (VIO) exposure times.

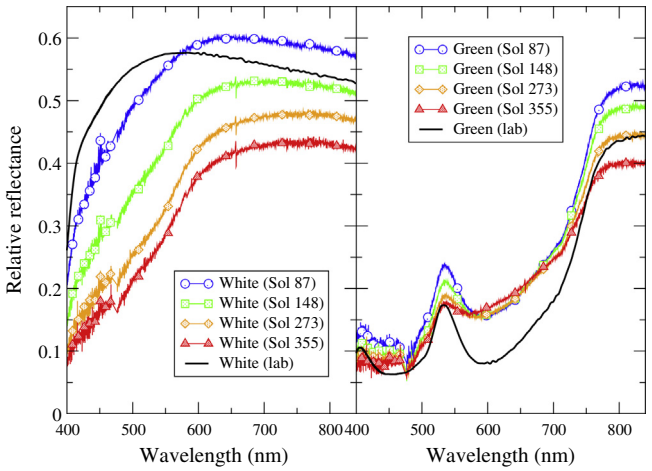

Fig. 9. ChemCam relative reflectance spectra of Mastcam calibration target white ring (*left*) and green color chip (*right*) acquired at four times compared to laboratory spectra (Bell et al., 2003). Gradual increase in dust coatings is evident on both surfaces. Symbols plotted on ChemCam spectra every 200th channel. (For interpretation of the references to color in this figure legend, the reader is referred to the web version of this article.)

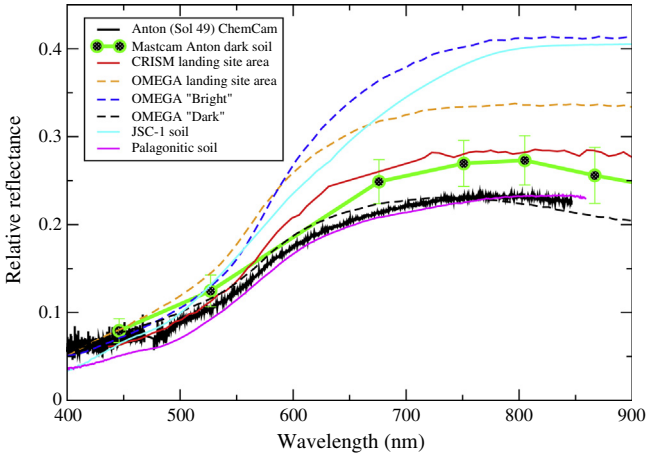

Fig. 10. Comparison of ChemCam relative reflectance spectrum of dark soil "Anton" (Sol 49) to Mastcam spectrum of same soil (Bell et al., 2013), a CRISM spectrum of the landing site region (Seelos et al., in preparation), average "bright" and "dark" OMEGA spectra of Mars (Ody et al., 2012) and an average spectrum of the landing site region (Gondet et al., 2013; Bibring et al., 2004), as well as laboratory spectra of the Mars analog soil JSC-1 analog soil (wet-sieved <45 mm; Johnson and Grundy, 2001), and a palagonitic soil (dry-sieved <45 mm; Cloutis et al., 2008a). CRISM data from image FRS00028346 (January 13, 2013; L_s = 244, local time: 15:14). OMEGA data of the landing site region acquired January 25, 2013 (L_s = 251, local time: 16:15). (For the interpretation of the references to color in this figure legend, the reader is referred to the web version of this article.)

Ming et al., 2013) are the highest relative reflectance materials observed (e.g., Rapitan, Sol 135). Rocks that were brushed by the Dust Removal Tool (DRT) (i.e., Wernecke_2, Sol 183, Cumberland, Sol 293) or broken by rover wheels (Nanok2, Sol 184) exhibit a lack of a 535 nm band and less steep ferric absorption edge, as do the drill tailings (John_Klein_DT, Sol 183; Cumberland_DT, Sol 281). These spectral features are consistent with a relative lack of crystalline ferric oxides. Downturns in the spectral slopes past 600 nm (particularly past 750 nm) observed in some targets are potentially related to near-infrared absorptions associated with low-Ca pyroxene (e.g., Ashuanipi, Sol 337). These spectral features are parameterized and discussed further in Sections 4.4 and 5.

As stated above, 3 ms exposure "dark" spectra were acquired as part of normal LIBS experiments. Fig. 12 shows comparisons of 3 ms spectra and dedicated passive spectra for three targets with high, intermediate, and low relative reflectance (cf. Fig. 11). Except for some variations in the VIO spectrometer (<470 nm), spectra acquired at the 3 ms exposure time provided sufficiently similar signal-to-noise spectra as the dedicated spectra to warrant their use. This expanded the available number of ChemCam passive spectra greatly, given that dark spectra were acquired with all standard LIBS measurements.

We note in Fig. 12 that the spectral region <500 nm in the VNIR data tends to exhibit a slight rollover towards shorter wavelengths that is not observed in laboratory data or Mars orbital datasets. This is likely an artifact caused by lower sensitivity of the VNIR spectrometer in this region owing to the spectrometer coating outgassing during the MSL cruise to Mars. Such optical throughput losses had been identified in thermal vacuum testing of the instrument prior to launch. This was corrected after landing by using empirical analyses of passive engineering spectra, but residual effects are manifested by slight downturns in relative reflectance shortward of ~500 nm, resulting in minor apparent relative reflectance offsets between the VNIR and VIO spectrometer spectral regions.

4.3. Dust coating effects

4.3.1. Surface targets

Nearly all the ChemCam passive spectra were acquired at locations that had been previously exposed to multiple laser shots as part of the LIBS analyses. Because the impact of the laser pulse redistributes fine grains and exposes subsurface materials (e.g., Graff et al., 2011), it was important to investigate the influence of the laser pulse on the relative reflectance spectra. Two experiments analyzed these effects on both a soil (Crestaurum2, Sol 84) and a rock surface (Duncan_Lake, Sol 111). In each experiment, six locations were analyzed using two data acquisition methods: (i) "dark" spectra acquired of an undisturbed surface, followed by either 30 laser shots (Locations 1 and 4) or 10 laser shots (Locations 2 and 5), followed by dark spectra; and (ii) dark spectra acquired before each of 10 laser successive single laser shots at the same target (Locations 3 and 6). Fig. 13 shows the resulting spectra for both experiments, and Fig. 14 shows the before and after RMI image mosaics of each area. In the Crestaurum2 soils, the effects of the hole created by the laser shots dominated the decrease in reflectance compared to the Duncan_Lake rock, where the removal of dust was the dominant cause for darkening. The number of laser shots (30 vs. 10) had less effect on the soil than the rock surface. There was a steady decrease in reflectance in Crestaurum2 for each of the 10 successive laser shots on Location 3, whereas only minor decrease in reflectance were observed for the Duncan_Lake surface (Fig. 13d). The darkening effect of the laser shots in the RMI images of Duncan_Lake appears to remove substantial amounts of dust. However, comparison of the relative reflectance spectra of the post-laser regions to laboratory spectra of basaltic samples coated with difference thicknesses of JSC-1 Mars analog soil (Johnson and Grundy, 2001) suggests the equivalent of ~30–50 μm of residual dust compared to a smooth basaltic surface.

At the distance of ChemCam to Crestaurum2 (2.68 m) on Sol 84, the 0.65 mrad spectrometer FOV corresponded to 1.75 mm diameter. Measurements of the hole diameters on the RMI images shown in Fig. 14 average ~1.35 mm, which represents ~60% of the area covered by the spectrometer FOV. As such, soil measurements can be partially influenced by a shade component (i.e., a greater diffuse reflectance contribution) in their relative reflectance spectra when coherent holes are formed. Hole formation does not always occur, as holes may collapse or incompletely form depending on the nature of the soil, its angle of repose, grain size, and in the case of drill tailings the thickness of the tailings deposit.

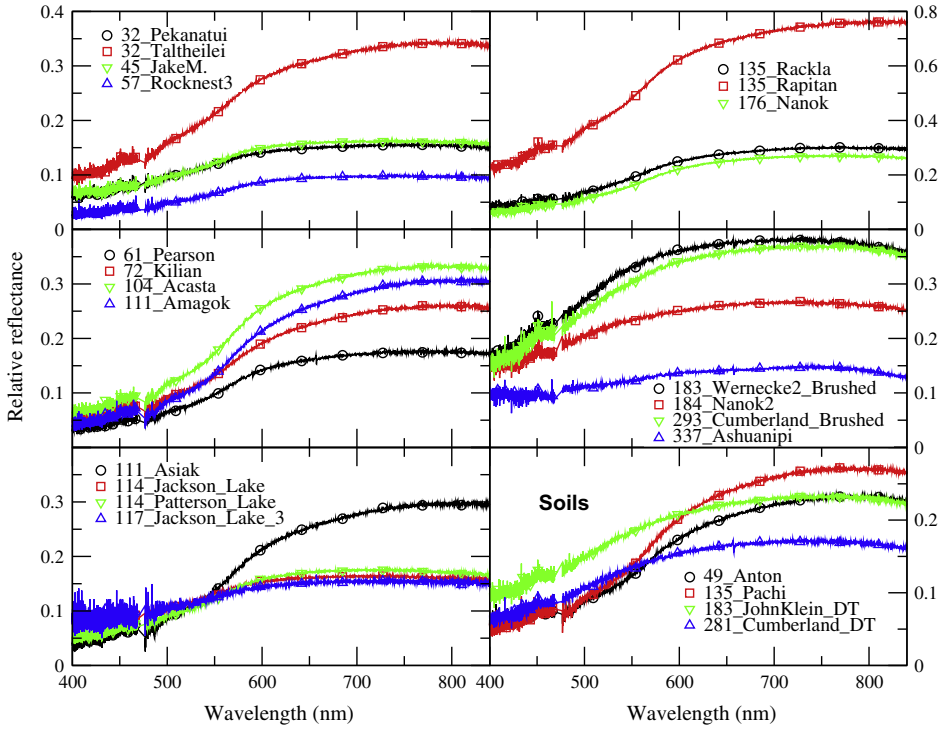

Fig. 11. ChemCam relative reflectance spectra from dedicated observations (Table 4). Note variable relative reflectance scales on each plot. Symbols plotted on ChemCam spectra every 200th channel.

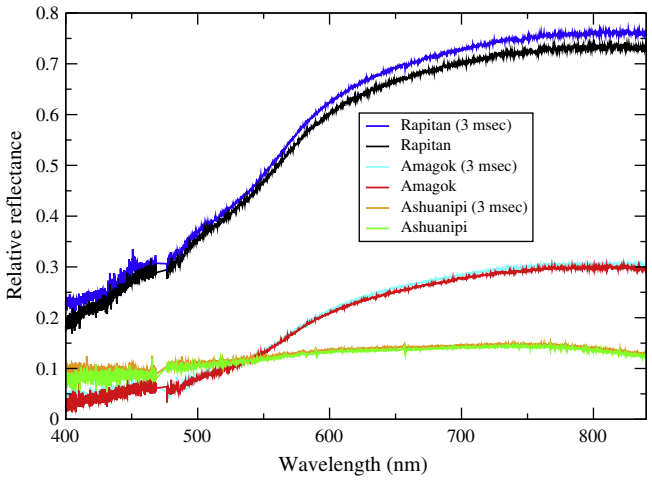

Fig. 12. Comparison of three dedicated vs. "dark" ChemCam passive spectra of same location, demonstrating overall similarity of 3 ms dark exposures to longer exposure observations. (For the interpretation of the references to color in this figure legend, the reader is referred to the web version of this article.)

4.3.2. Calibration targets

The influence of dust on the CCCT Target #11 (Fig. 6) and Mastcam calibration target white ring and green color chip (Fig. 9) was described above. Additional observations of the sweep magnet area under the white ring of the Mastcam calibration target provided insight to the differences between magnetic and non-magnetic dust. The combined observations of the black, gray, and white rings of the Mastcam calibration target (and the CCCT Targets #5, #6, and #11) also provide a means to track dust variability and will eventually be incorporated into dust-correction algorithms (Section 6; Tables 2 and 3).

The white ring magnet region was a more challenging observation because the distance to that portion of the Mastcam calibration target was a few millimeters below the close focus limit of ChemCam. Hence, the RMI images shown in Fig. 7c–g are somewhat out of focus and the observation footprint of the spectrometers is ~1.5 mm (about twice the size of a well-focused observation at the 1.17 m distance). Nonetheless, the relative reflectance spectra acquired from those locations demonstrate important differences related to the nature of the dust. Fig. 15 shows representative spectra from the Sol 193 observation in which the center of the magnet ("Center1") is compared to the other four locations that incorporate the center plus some of the low albedo ring of magnetic dust ("Magnet2"), mainly the magnetic dust ("Magnet3"), the magnetic dust plus some of the standard white ring target ("Ring4"), and the white ring target alone ("Ring5"). Also shown for comparison is the laboratory spectrum of the white ring material (Fig. 9), which demonstrates that even the Center1 region is not completely free of dust, as evidenced by its lower reflectance in the 400–650 nm region. This implies that some of the airfall-deposited dust on the calibration target is non-magnetic, consistent with previous work on the nature of dust deposition on calibration targets (e.g., Hviid et al., 1997; Bertelsen et al., 2004; Goetz et al., 2005; Vaughan et al., 2010; Drube et al., 2010). The sweep magnet center certainly exhibited the highest relative reflectance, however, and demonstrated a much shallower 535 nm absorption band than the Ring5 area, consistent with its lack of lower albedo and more ferric components. Indeed, previous studies have concluded that the strongly magnetic component in martian dust likely contains magnetite, which would contribute to the observed lower relative reflectance of the Magnet3 region, as well as the weak ~550 nm band.

Fig. 16 compares spectra of the center of the sweep magnet (divided by the cosine of the solar incidence angle) for five different sols and to the laboratory spectrum of the white ring material. Overall, the change in spectral shape of this region over time is relatively minimal. Most differences likely result from small targeting

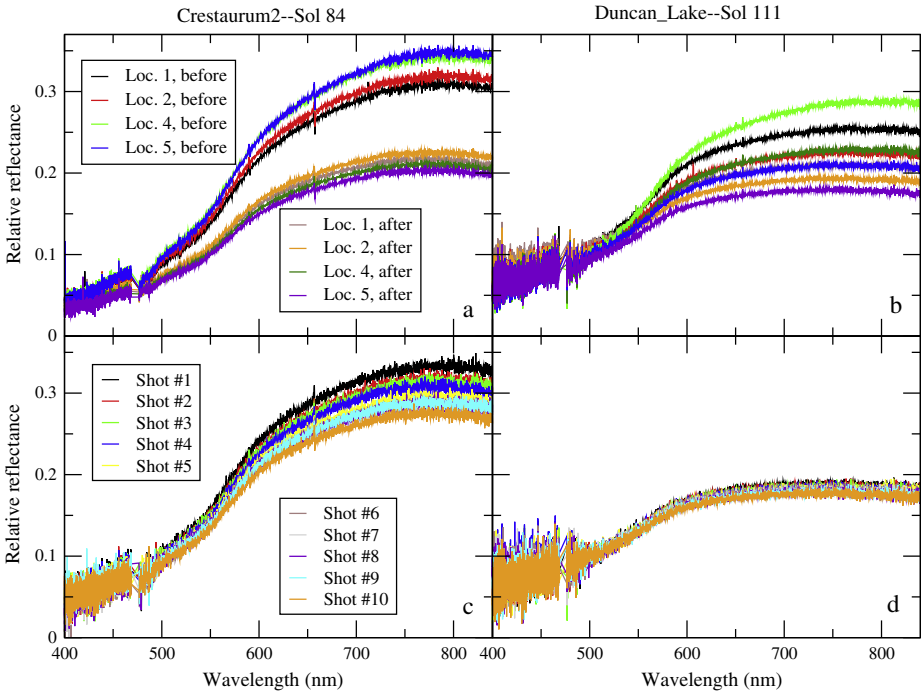

Fig. 13. ChemCam passive relative reflectance spectra (3 ms observations) taken of soil Crestaurum2 on Sol 84 (a) and rock Duncan_Lake on Sol 111 (b) both before and after 30 laser shots (Locations 1 and 4), and before and after 10 laser shots (Locations 2 and 5) (legend applies to both plots) (see Fig. 14 for RMI images). Decrease in reflectance after shots in Crestaurum2 soil is attributable mainly to shadows from LIBS-generated holes, whereas reflectance drop after shots on Duncan_Lake rock is due to dust removal. Plots (c and d) show results from spectra acquired after a series of ten successive laser shots at the same location (Location 3). Continual decrease in reflectance with each shot attributable to loss of dust on both targets, plus increased shadowing from LIBS holes on Crestaurum2. Noisier VIO spectrum for Duncan_Lake spectra results from higher instrument temperature (+8 °C) compared to Crestaurum2 (−9 °C). (For the interpretation of the references to color in this figure legend, the reader is referred to the web version of this article.)

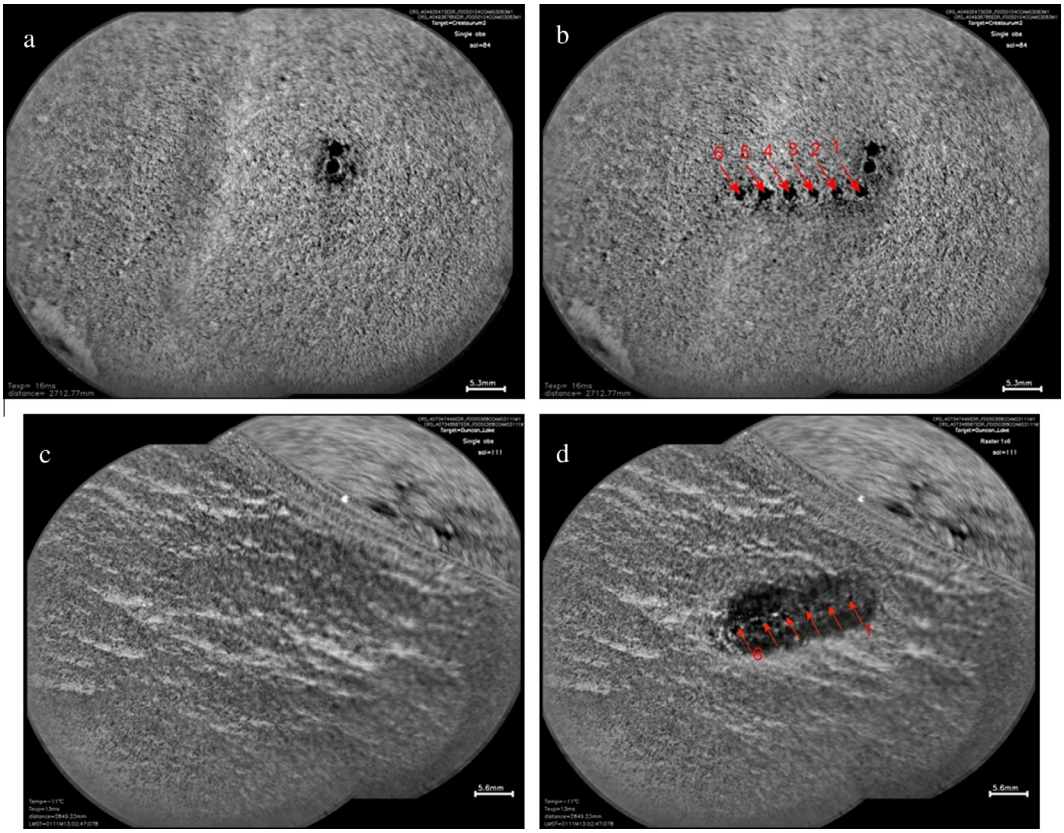

Fig. 14. RMI image mosaics of Crestaurum2 soil before (a) and after (b) laser shots on six locations, as labeled (CR0_404935473EDR_F0050104CCAM03083, CR0_404936786EDR_F0050104CCAM03083). (Two laser holes in (a) result from previous soil measurements described by Meslin et al. (2013).) Duncan_Lake images shown before (c) and after (d) laser shots on six locations, as labeled (CR0_407347449EDR_F0050388CCAM03111; CR0_407348687EDR_F0050388CCAM03111).

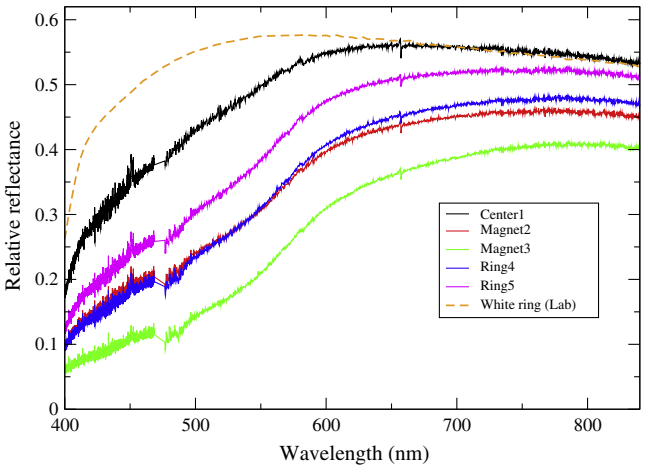

Fig. 15. ChemCam relative reflectance spectra of the Mastcam sweep magnet area acquired from Sol 193 3-ms exposure observations, including the center, magnetic dust ring, and exterior, standard white calibration target (cf. Fig. 7c–g); see text for details. Also shown is the laboratory bidirectional reflectance spectrum of the white ring material (cf. Fig. 9). (For the interpretation of the references to color in this figure legend, the reader is referred to the web version of this article.)

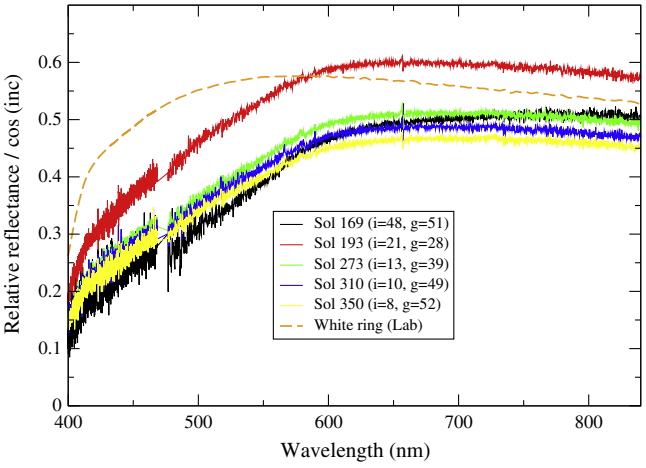

Fig. 16. Chemcam relative reflectance spectra (divided by cosine of the incidence angle i) of the center of the sweep magnet under the Mastcam calibration target white ring (Fig. 7c) for 5 different sols (3-ms exposures) compared to laboratory spectrum of white ring material (cf. Fig. 9). Lower phase angle (g) of Sol 193 observation may be responsible for elevated reflectance values. (For the interpretation of the references to color in this figure legend, the reader is referred to the web version of this article.)

offsets among observations owing to slight fluctuations in pointing repeatability at such fine scales. The elevated relative reflectance values for the Sol 193 observation may result from its somewhat lower phase angle compared to the other observations. For comparison, Fig. 17 shows spectra from the black, gray, and white Mastcam calibration target rings acquired on Sol 321, demonstrating the dusty nature of the targets compared to their laboratory spectra. Despite the dust contamination, the three targets still can be distinguished by their overall reflectance values. This allows their usage for ongoing dust correction efforts that are discussed in Section 6.

4.4. Spectral parameter analyses

For all ChemCam passive spectra acquired of rocks and soils at 3 ms exposure times, we calculated simple parameters such as

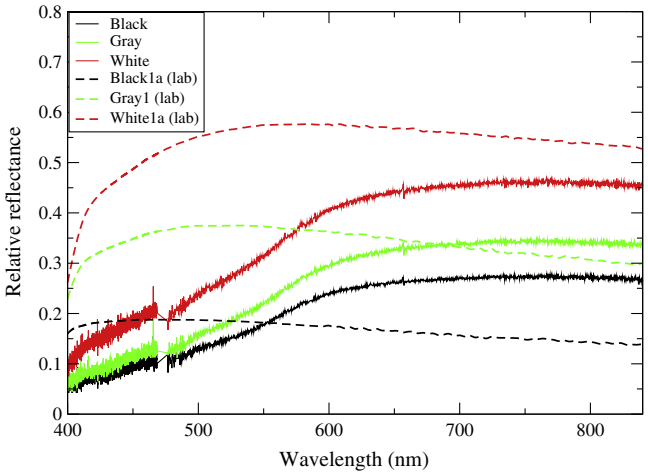

Fig. 17. ChemCam relative reflectance spectra acquired from the Sol 321 3 ms exposure observations of the black, gray, and white Mastcam calibration target rings compared to bidirectional laboratory reflectance of the same materials. Airfall-dust deposits coating the calibration target materials alter their spectra appreciably (compare Fig. 9a). (For the interpretation of the references to color in this figure legend, the reader is referred to the web version of this article.)

Table 5
Spectral parameters used in this study.

Parameter	Description
BD535	535 nm band depth (500–600 nm continuum)
BD600	600 nm band depth (535–670 nm continuum)
S6084	Slope between 600 and 840 nm
S7584	Slope between 750 and 840 nm
R6084	Ratio of 600/840 nm
R6744	Ratio of 670/440 nm
R7584	Ratio of 750/840 nm

band ratios, band depths, and spectral slopes to quantify specific features or trends and identify endmember spectra. Here we adopt the spectral parameters listed in Table 5, many of which have heritage from previous multispectral studies (e.g., McSween et al., 1999; Bell et al., 2000; Farrand et al., 2006, 2007, 2008a,b). Schematic examples of each spectral parameter are shown in Fig. 18. For each wavelength listed we extracted the average value within ±5 nm to avoid complications from spurious single channels. These parameters were selected to discriminate between the main spectral features observed in the ChemCam data, namely the slopes of the visible and near-infrared regions, and the strength of a shallow band near 535 nm and the shoulder near 600 nm. The 535 nm band depth (BD535) is sensitive to the presence of crystalline ferric oxides (e.g., Morris et al., 1985, 1997). We selected the 500–600 nm region for the continuum used in computing this band depth in order to avoid somewhat noisier data in the <500 nm region described above. The BD600 parameter is related to the strength of the short wavelength ferric oxide absorption edge; selecting the 535–670 nm region for the continuum allowed for more direct comparisons to the 670/440 nm ratio (R6744). The near-infrared region was characterized by differences in the slope and ratio between 750 nm and 840 nm (S7584, R7584, respectively), and between 600 nm and 840 nm (S6084, R6084). These parameters are intended mainly to be illustrative (but not comprehensive) of the spectral variability in the rock and soil datasets described above.

Fig. 19 shows comparison of these spectral parameter calculations for all rock observations. Particular classes of targets that were noted to cluster in specific regions on one or more of these plots are designated, and Table 6a lists the representative targets used for each class. These endmembers are intended only to be

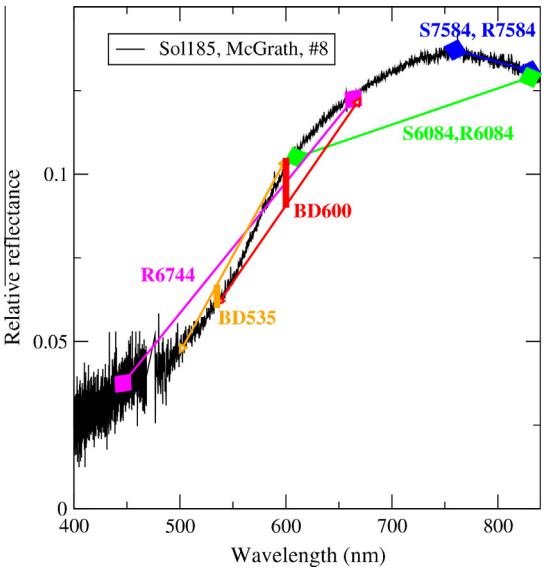

Fig. 18. Examples of spectral parameters listed in Table 5, shown on a representative spectrum from the Sol 185 McGrath target (location #8).

examples of the spectral variations that can be discriminated among units sampled by ChemCam. They include: "Exposed" rocks that were either brushed by the DRT or fractured by the rover wheels; "Dark" rocks that included samples with low relative reflectance combined with significant near-infrared spectral slopes (i.e., low S7584 values); "Bradbury" samples from within the immediate landing zone (Sols 1–20); "Ridges" representative of some of the prominent, MgO-rich, raised ridge surfaces (e.g., Léveillé et al., submitted for publication); "Red" surfaces typical of relatively high reflectance surfaces dominated by red, dusty surfaces; and "Veins" representative of the calcium sulfate-rich veins observed by Curiosity at multiple locations (e.g., Nachon et al., submitted for publication, 2014). To help discern the extent to which variable dust coatings cause some of the observed spectral parameter trends, we also show the spectral parameters computed for the suite of laboratory dust-coated basaltic samples studied by Johnson and Grundy (2001). In that study a cored sample of basaltic andesite (SP Flow, AZ, labeled *SPF*) was deposited with ~17 to ~122 μm thicknesses of JSC-1 Mars analog soil (wet-sieved to <45 μm, labeled *JSC1*).

Fig. 20 shows a similar set of plots for all soils, in which the representative target types are listed in Table 6b. This includes: "Bright" soils that typically have high relative reflectance

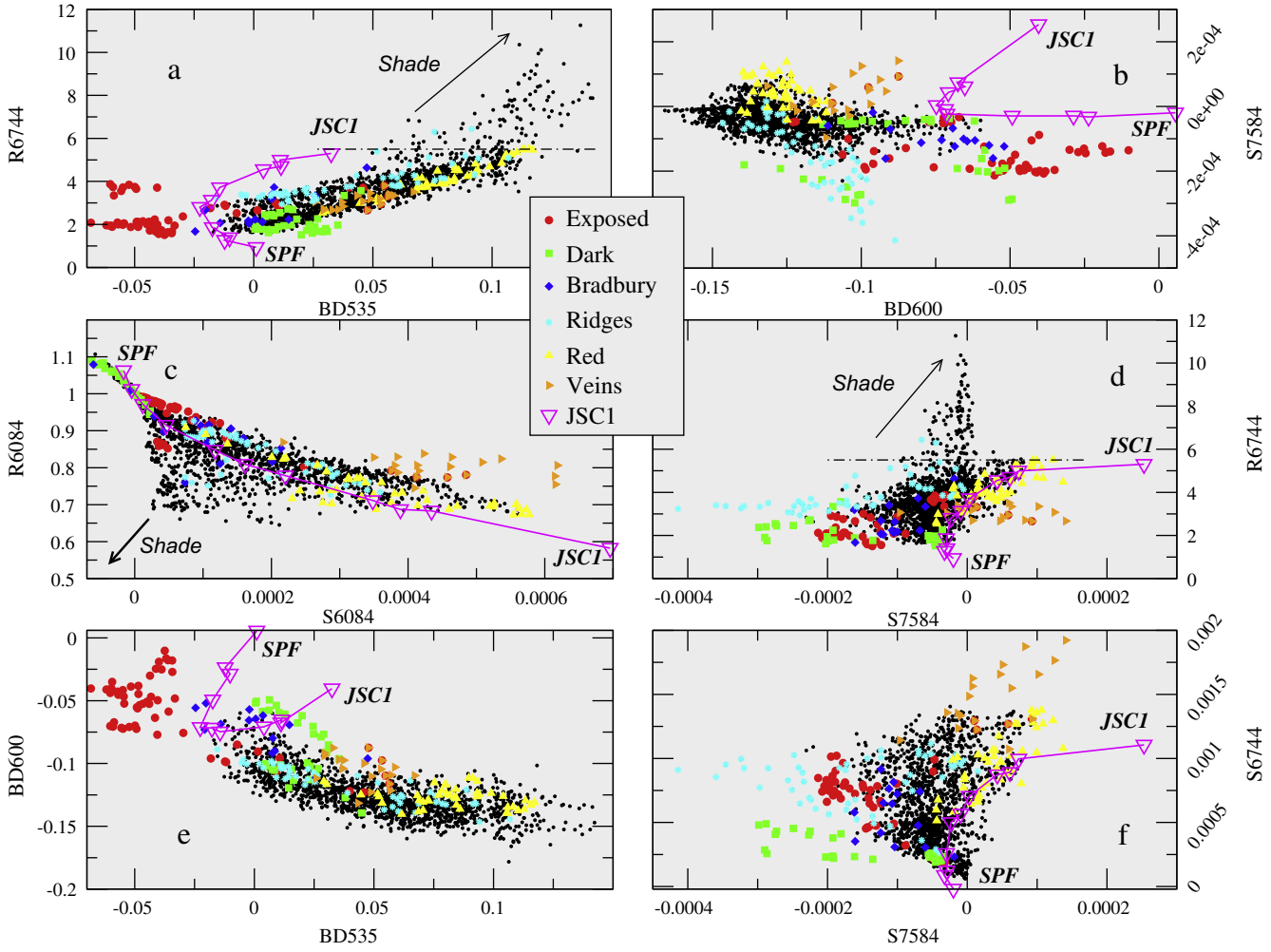

Fig. 19. Comparisons of spectral parameters (Table 5) for all rock targets; (a) BD535 vs. R6744; (b) BD600 vs. S7584; (c) S6084 vs. R6084; (d) S7584 vs. R6744; (e) BD535 vs. BD600; and (f) S7584 vs. S6744. Highlighted points are from representative target types listed in Table 6a and discussed in text. Arrows point toward stronger trends of "shade" associated with shadowed regions. R6744 values >5.5 (marked with a dot-dash line) are typical of shadowed regions, as are low values of S6084 and R6084 that fall off the main trendline. Also shown are parameter values for a basaltic rock (*SPF*) and a suite of samples coated with variable average thicknesses (17, 19, 27, 42, 53, 61, 81, 106, and 122 μm) of Mars analog soil (*JSC1*) from Johnson and Grundy (2001). (For the interpretation of the references to color in this figure legend, the reader is referred to the web version of this article.)

Table 6a
Target types and representative members: Rocks.

Veins	Raised ridges	Dark rocks	Red rocks	Exposed surfaces	Bradbury landing zone
Rapitan [1135; 1.0 °C]	John_Klein [3165; *4*, *5*, *6*; 0.2 °C]	Ashuanipi [3337; −6.7 °C]	Rifle [1119; 3.5 °C]	Wernecke1_Brush [1172; −1.7 °C]	Coronation [2103; 0.1 °C]
Tukarak [4165; *1*, *2*, *4*, *7*; 2.5 °C]	McGrath [1193; *1–5*; −2.8 °C]	La Reine [1346; −8.8 °C]	Keskarah [1124; 0.5 °C]	Werneck2_Brush [1183; −1.7 °C]	Link [2027; 2.0 °C]
Measles Point [1305; *9*; −2.5 °C]	McGrath4 [1226; −3.3 °C]	Black Trout [1349; −9.0 °C]	Rocknest3 Top [1088; 4.8 °C]	Tukarak [4165; 1.8 °C]	Goulburn {2, 3, 4, 7, 8} [1014, 2014, 1015, 2019, 4019; −1.2 °C, −0.6 °C, −0.9 °C, 0.4 °C, 2.3 °C]
Mavor [2160; 5, 6; −1.9 °C]	McGrath5 [2234; −0.4 °C]	Mallard Lake [3349; −7.6 °C]		Cumberland Brush [1292; 2.8 °C]	Mara [5015; 0.7 °C]
Richardson2 [2130; *1*, *2*, *4*; 1.5 °C]	Lady_Nye {1, 2, 3} [6284, 1286, 2286; −6.8 °C, −5.9 °C, −7.3 °C]			Nanok2 [6184; 0.7 °C]	Stark [3015; 0.1 °C]
Kazan [1188; *6*; −1.9 °C]	Lady_Nye4 [1290; *1*, *2*, *4–7*, *14–15*; 2.8 °C]			Cumberland Drillhole [7284; −5.8 °C][a]	Mara_1 [1019; −0.6 °C]

Numbers in curly brackets ({}) represent numbered versions of same target name. Square brackets include [ChemCam sequence identification number; *location number(s)* within raster if not all locations used; average instrument temperature during observations].
[a] Includes drill tailings and shots in shadowed drill hole.

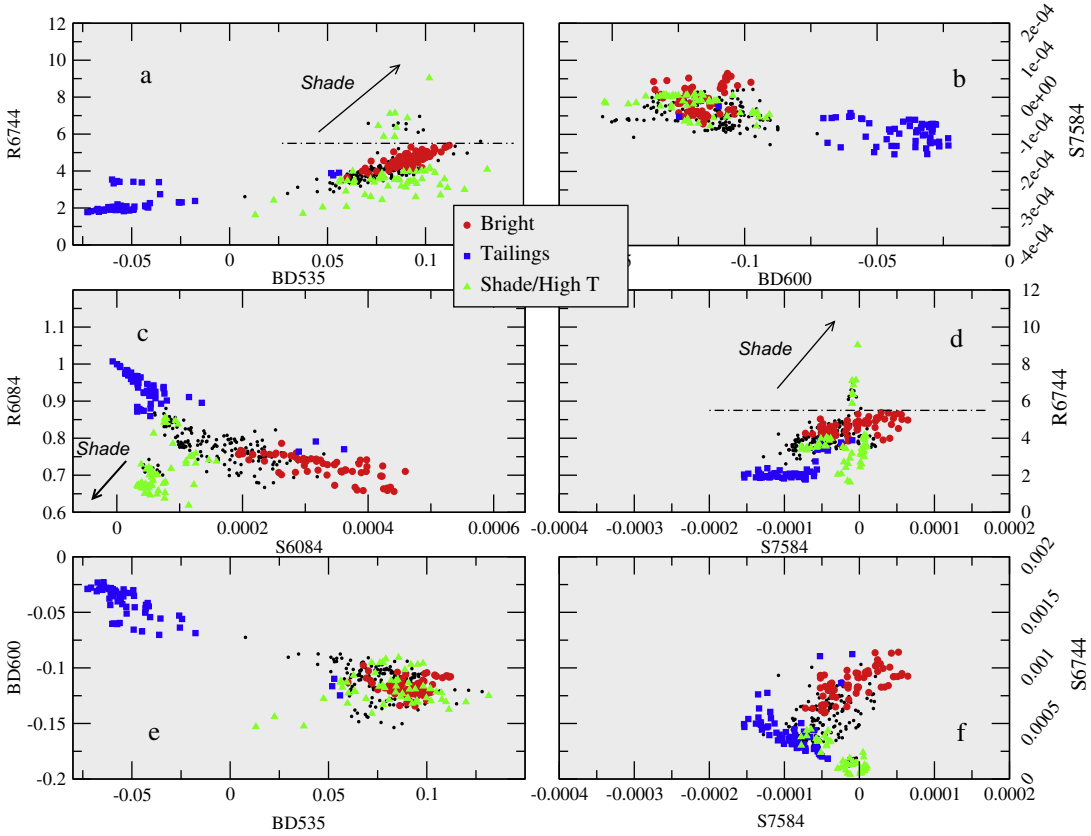

Fig. 20. Comparisons of spectral parameters (Table 5) for all soil targets; (a) BD535 vs. R6744; (b) BD600 vs. S7584; (c) S6084 vs. R6084; (d) S7584 vs. R6744; (e) BD535 vs. BD600; and (f) S7584 vs. S6744. Highlighted points are from representative target types listed in Table 6b and discussed in text. Arrows point toward stronger trends of "shade" associated with shadowed regions. R6744 values >5.5 (marked with a dot-dash line) are typical of shadowed regions, as are low values of S6084 and R6084. (For the interpretation of the references to color in this figure legend, the reader is referred to the web version of this article.)

consistent with dusty surfaces; "Tailings" that include the drill tailings from the John_Klein and Cumberland drill locations; and "Shade/High T" samples that either represent locations dominantly shadowed (typically soils disturbed by the rover wheels), or targets acquired at elevated instrument temperatures (e.g., >5 °C). For the latter observations, higher channel-to-channel noise levels can create artifacts in the low-wavelength region (despite the 10 nm-sampling used to calculate the spectral parameters). This can result in anomalously high 440 nm values, which artificially reduces the R6744 and S6744 values (Fig. 20d and f). Fig. 21 shows examples of the relative reflectance spectra of the rock target types used in Fig. 19, demonstrating the range of spectral variability documented

Table 6b
Target types and representative members: Soils.

Bright soils	Drill tailings	Shade (or high temp.)
Kanyuak [1123; 0.8 °C]	John_Klein Drill Tailings {1, 2, 3, 4} [2183, 2195, 2227, 1234; 0.5 °C, 11.6 °C, −2.7 °C, −2.4 °C]	Sutton_Inlier [2169; 11.5 °C]
Coppermine [1097; 1.4 °C]	John_Klein Drill hole [1227; −3.7 °C]	Richmond_Gulf [1194; 13.4 °C]
Pachi [3135; 7; 3.0 °C]	Cumberland Drill Tailings [1281; −6.4 °C]	Epworth3 [2084; −9.0 °C]
Kam [3043; 1.3 °C]	Cumberland Drill Tailings 2 [2289; 3.3 °C]	Kenyon [2097; 2.2 °C]
Crestaurum2 [3083; −9.0 °C]		Young_Point [5316; 6.7 °C]

Numbers in curly brackets ({}) represent numbered versions of same target name. Square brackets include [ChemCam sequence identification number; *location number(s)* within raster if not all locations used; average instrument temperature].

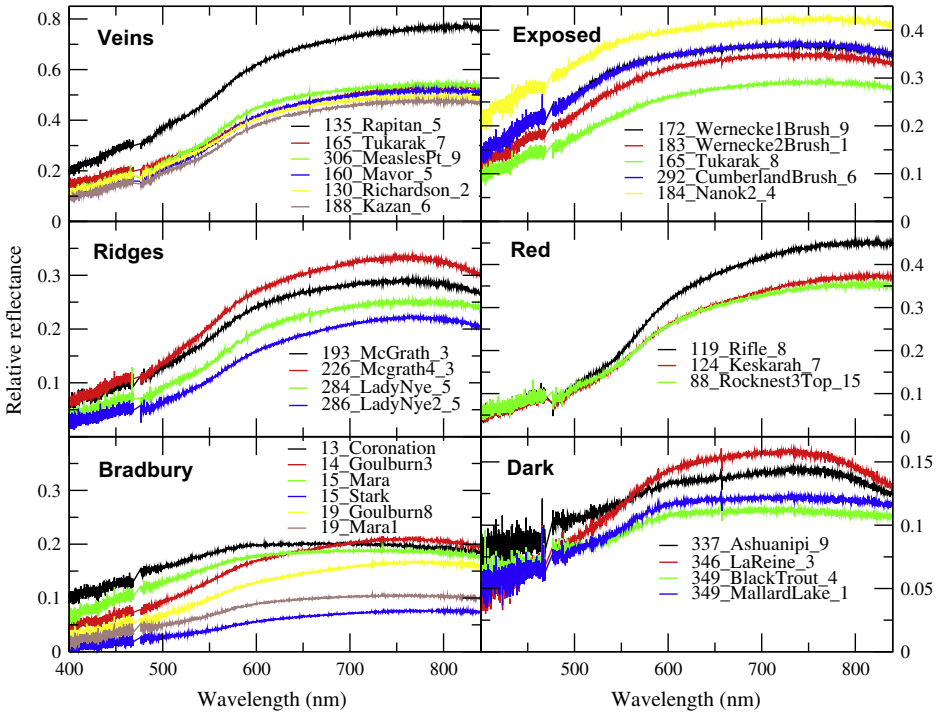

Fig. 21. Example ChemCam relative reflectance spectra of representative rock target types used in Fig. 19 (cf. Table 6a), demonstrating range of spectral variability. Legend descriptors correspond to Sol number, target name, and location number for multiple-location rasters. Note variable reflectance scales on each plot. (For the interpretation of the references to color in this figure legend, the reader is referred to the web version of this article.)

by the spectral parameters. Fig. 22 shows similar examples of spectra for the three soil target types.

5. Discussion

ChemCam relative reflectance spectra of pristine and disturbed materials at the Curiosity landing site demonstrated a variety of visible/near-infrared spectral features that can be used to help constrain compositional and mineralogical interpretations of rocks, soils, drill tailings, and airfall dust. Here we discuss the specific classes of materials presented above, and make comparisons to laboratory spectra of candidate minerals and soils. Because of the limited spectral range available (400–840 nm), multiple mineral candidates exhibiting optically equivalent features are possible, particularly amidst the presence of airfall-deposited dusts and windblown soils. More detailed spectral mixing models could refine these results further, but are beyond the scope of the current preliminary effort. As mentioned above, some target points were fully or partially shadowed during acquisition of passive spectra. Typically these spectra exhibit R6744 values >5.5, low S6084 and R6084 values, and 750 nm relative reflectances <0.05, as shown in Figs. 19–22. Elevated instrument temperatures (5–10 °C) often occurred in late-afternoon measurements and resulted in noisy spectra below 500 nm (e.g., Fig. 22).

Because the Curiosity landing site was known from orbital measurements to be relatively dusty (e.g., Buz and Ehlmann, 2013), many of the surfaces observed by ChemCam were variably coated with dust that diminished the strength of spectral features. The Red rock target type (Figs. 21 and 23) and the Bright soil type typical of such surfaces share high 535 nm band depths (BD535), negative 600 nm band depths (BD600) and reddened spectral slopes (R6744, S6744) as well as positive near-infrared slopes and ratios (S6084, S7584). These are consistent with fine-grained JSC-1 Mars analog soils and the OMEGA spectrum of typical "bright" (dusty) surfaces (Fig. 10). For comparison, some of the targets acquired in the Bradbury landing zone "blast" area have lower relative reflectance values, some of the highest BD600 values and lowest BD535 values, and slightly negative near-IR slopes, all consistent with the darkening effects observed in post-landing orbital images. Comparison of the spectral parameters to those of laboratory dust-coated samples of Johnson and Grundy (2001) suggests that the Bradbury rocks may have <50 μm of dust coatings on average, whereas the Red rock types likely have coatings >100 μm (e.g., Fig. 19c).

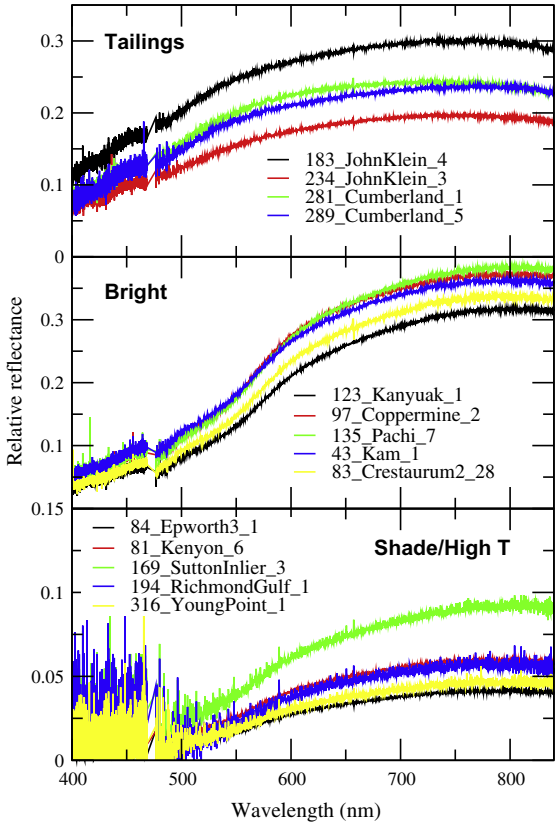

Fig. 22. Example ChemCam relative reflectance spectra of representative soil target types used in Fig. 20 (cf. Table 6b). Legend descriptors correspond to Sol number, target name, and location number for multiple-location rasters. Note variable reflectance scales on each plot. (For the interpretation of the references to color in this figure legend, the reader is referred to the web version of this article.)

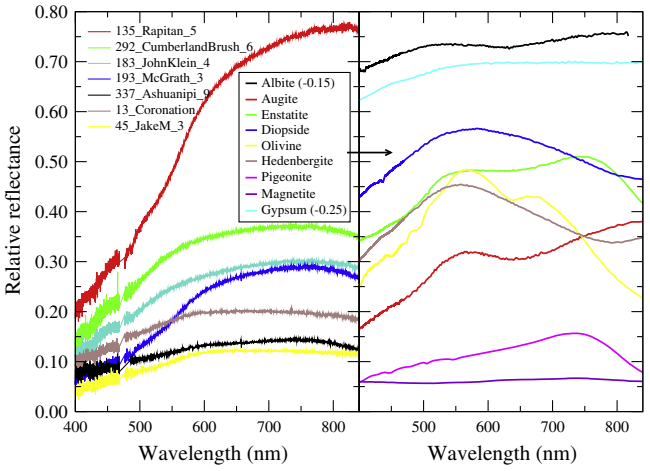

Fig. 23. Representative ChemCam relative reflectance spectra (*left*) of target types compared to laboratory reflectance spectra of candidate minerals (*right*). Legend descriptors in left pane correspond to Sol number, target name, and location number for multiple-location rasters. Mineral names in right pane correspond to spectra from the USGS spectral library (Clark et al., 2007) as follows: albite (gds30.34w6; $NaAlSi_3O_8$); augite (ws592.3247; $(Ca,Na)(Mg,Fe,Al,Ti)(Si,Al)_2O_6$); enstatite (NMNH128288.7435; $Mg_2Si_2O_6$, cited to have a "higher iron content than pure enstatite"); diopside (NMNHR18685.7035; $CaMgSi_2O_6$); olivine (NMNH137044.17191; $(Mg,Fe)_2SiO_4$; Fo_{92}); hedenbergite (NMNH119197.9218; $CaFe^{2+}Si_2O_6$). Pigeonite is from the RELAB database (c1pp36, $En_{55}Fs_{41}Wo_4$), and magnetite (MAG110; $Fe_2^{3+}Fe^{2+}O_4$) and gypsum (SPT207; $Ca(SO_4)\cdot 2(H_2O)$) are from the Planetary Spectrophotometer Facility data base (Cloutis et al., 2006b) Offsets noted parenthetically for albite and gypsum spectra. (For the interpretation of the references to color in this figure legend, the reader is referred to the web version of this article.)

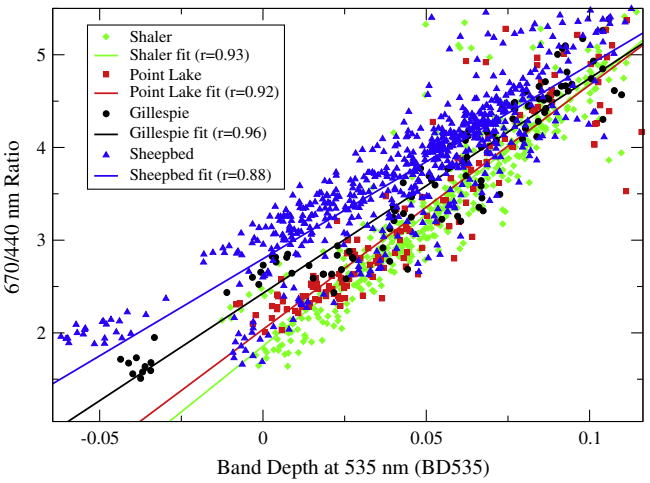

Fig. 24. Spectral parameters from Fig. 19a, classified by stratigraphic unit member. Data restricted to R6744 values <5.5 to minimize effects of shaded targets. Linear fits to each data set shown, along with correlation coefficient (*r*). (For the interpretation of the references to color in this figure legend, the reader is referred to the web version of this article.)

The Dark rock types exhibited low red/blue ratios and slopes, slightly positive BD535 values, some of the most negative near-infrared slopes, and the highest R6084 ratios. Two of these samples are particularly compelling because of their significant near-infrared downturns beginning near 750 nm: Ashuanipi (Sol 337) and La Reine (Sol 346). La Reine is slightly dustier (as evidenced by a more prominent ferric absorption edge <600 nm) compared to the flatter visible wavelength spectra associated with Ashuanipi. The MgO-raised ridge materials (Ridges) also exhibited downturns in the near-infrared (S7584) despite their more typical visible wavelength features. Depth profiles conducted on some of these targets acquired passive spectra between each of four sets of 150-shot laser observations at the same location. Such passive spectra of Lady_Nye3 (Sol 286, not shown here) exhibited a slight increase in the near-infrared slope and a decrease in near-infrared relative reflectance with depth.

Fig. 23 provides spectral context for these observations by comparing examples of ChemCam relative reflectance spectra for the main target types with laboratory spectra of representative minerals. The nonlinear contribution of darkening agents such as magnetite is likely responsible for differences between laboratory spectra and martian surface spectra, in addition to residual dust deposits within a given field of view. The downturns in near-infrared reflectance described above begin around 750 nm, which is more consistent with orthopyroxenes (e.g., enstatite) than olivine or clinopyroxenes (e.g., hedenbergite).

The calcium sulfate-rich vein materials observed by Curiosity (e.g., Rapitan) exhibit the highest reflectance of all targets. Indeed, whenever LIBS measurements from ChemCam detected high-Ca and potential high-S, such locations nearly always exhibited elevated reflectance. Gypsum, bassanite, and anhydrite reflectance spectra are typically characterized by high-reflectance, relatively featureless spectra in the 400–840 nm region (Fig. 23). However, all Vein measurements were contaminated to some degree by residual dust coatings within the field of view, as evidenced by the ferric absorption edge <600 nm.

The Exposed targets (brushed and fractured rocks) exhibited unique spectral features, with the lowest BD535 and among the lowest R6744 ratio values, the least negative BD600 values, and a slight negative near-infrared slope. These spectral features are

matched by the drill tailings measurements at the John_Klein and Cumberland targets. The grayish color of both target types in Mastcam images is consistent with the spectra shown in Fig. 21, and is indicative of the much more ferrous nature of these materials (e.g., Vaniman et al., 2013).

The stratigraphic units mapped in the Yellowknife Bay area included in descending order the Glenelg member (comprising the Bathurst_Inlet, Shaler, and Point Lake outcrops), Gillespie Lake, and Sheepbed members in (e.g., Stack et al., 2013; Grotzinger et al., 2013; Anderson et al., 2015; Vaniman et al., 2013; McLennan et al., 2013). Orbital imaging showed the Sheepbed member to be light-toned and somewhat redder than the other units. Grouping the targets from Fig. 19a (BD535 vs. R6744) by stratigraphic unit reveals that most materials within the Sheepbed member indeed exhibit the highest R6744 values. Furthermore, a distinct trend is observed in which the targets become progressively redder farther east into Yellowknife Bay, as shown in Fig. 24.

6. Conclusions and future work

6.1. Summary

The high sensitivity of the ChemCam spectrometers on the Curiosity rover allowed generation of relative reflectance spectra that accurately reproduced the laboratory visible/near-infrared spectra of onboard calibration targets. Ongoing airfall dust deposition on the calibration targets throughout the mission limited their utility. However, first-order calibrations using the relatively dust-free Sol 76 observation of the ChemCam Target #11 enabled a consistent data reduction method that resulted in the first high spatial and high spectral resolution visible/near-infrared measurements of the martian surface from a landed platform.

Multiple observations of the calibration targets effectively served as a means to monitor dust deposition on the rover, which increased substantially over the first year of the mission. Magnetic dust collected by the sweep magnet exhibited deeper ferric absorption bands than unfiltered airfall dust, consistent with previous studies. Although the center of the magnet region also exhibited some dust collection, observations suggest that it likely reached an equilibrium state.

Most surface spectra are consistent with orbital observations, exhibiting a steep ferric absorption edge shortward of 600 nm. However, a variety of rock and soil targets exhibit distinctive spectral features (assisted by the dust-clearing effect of the laser shots that often preceded passive spectra), such as the near-infrared downturns associated with the raised ridge materials (e.g., McGrath, Lady_Nye) (Fig. 21), and with some Dark rocks (e.g., Ashuanipi, La Reine). These spectral features may be associated with orthopyroxenes, although further spectral mixture analyses are warranted to better constrain mineral candidates. Brushed surfaces and drill tailings exhibited unique visible wavelength characteristics (e.g., absence of 535 nm band depths, low red/blue color ratios). Comparison of spectral parameter trends with laboratory dust-coating studies demonstrates that dust thickness differences among targets is a reasonable explanation for some of the visible wavelength spectral variations observed in the data sets shown here. Indeed, some of the first targets examined by ChemCam within the landing zone appear darker than similar rock types outside of the blast zone, suggesting the partial removal of surface dust coatings is likely responsible. The calcium-sulfate veins observed by Curiosity (e.g., Nachon et al., submitted for publication, 2014) are characterized by the most positive near-infrared slopes and largest relative reflectances observed by ChemCam. Dust contamination on these surfaces may explain the residual ferric absorption edge in their spectra, although minor structural Fe^{3+}-contamination cannot be ruled out. Overall, the ChemCam investigations of passive spectra provide a rich data set that supports the LIBS observations regarding the small-scale heterogeneity of martian surface materials. For example, the Tukarak area (Sol 165) sampled three different target types (Red, Vein, and Exposed) within a single raster measurement (cf. Fig. 21).

6.2. Future work

6.2.1. Spectral analyses

Although beyond the scope of the current work, comparisons of elemental compositions from ChemCam LIBS analyses to reflectance spectra would be a logical continuation of this work. In addition, the high spectral resolution afforded by ChemCam may enable investigation of narrower spectral reflectance features than are otherwise not observable by broadband, multispectral cameras such as Mastcam. For example, goethite exhibits Fe^{3+} spin-forbidden bands near 500 and 650 nm, whereas absorptions related to Fe^{2+}–Fe^{3+} charge transfers occur around 730 nm in phyllosilicates such as serpentine or saponite. Cloutis et al. (2006a) demonstrated that the position and shape of the 430 band (resulting from bonding in Fe^{3+} octahedral sites) can be used to discriminate different sulfates (Cloutis et al., 2008b). In addition, Cloutis (2002) and Cloutis et al. (2010) demonstrated that spin-forbidden bands due to Fe^{2+} and other cations in pyroxenes are diagnostic of composition, in particular the 506 nm Fe^{2+} band that can be used to constrain composition (Ca, Fe^{2+}) and structure (cf. Klima et al., 2007). Furthermore, serpentines also exhibit a 440 nm band resulting from tetrahedrally coordinated Fe^{3+} (e.g., Greenberger et al., 2013).

6.2.2. UV spectral region

The UV region below 400 nm is of interest because it has been largely underutilized for studies of the martian surface. One exception is the work of Bell and Ansty (2007), who demonstrated with Hubble Space Telescope observations that regions typically "bright" in the visible show a contrast reversal below about 340 nm with low albedo regions. Similar contrast reversals were observed by Clancy et al. (2006) using Mars Color Imager (MARCI) data from Mars Reconnaissance Orbiter (MRO). Bell and Ansty (2007) speculated that the larger concentration of Fe^{3+} in the dusty bright regions resulted in deeper Fe–O absorptions in the ultraviolet, thereby causing the contrast reversal. The main causes of spectral absorptions in the 200–400 nm region are intense Fe–O charge transfer (CT) absorptions, in addition to other metal–O CT bands (e.g., Ti, Mn, Ni). The Fe–O bands can arise from both Fe^{2+} and Fe^{3+}, although Fe^{3+}–O bands are up to 100 times stronger than Fe^{2+}–O bands, and can be sensitive to even small amounts (<0.01%) of Fe^{3+}. Cloutis et al. (2008a) demonstrated the utility of spectral ratios in distinguishing the depth of the Fe^{2+}–O CT band near 270 nm.

The UV spectrometer data were deferred in these analyses, mainly because the spectral reflectance of the CCCT Target #11 surface was near zero in this spectral region. Preliminary tests were done using Target #6 ("Kaolinite") as a proxy calibration target for the UV because it exhibits higher reflectance in the UV. Initial results suggest it could provide useful data at wavelengths down to ~300–400 nm. Methods using exoatmospheric solar irradiance spectra to reduce UV data were also examined, but channel-to-channel variations in the ChemCam UV spectra hindered initial attempts. Ongoing analyses of passive mode investigations of Mars atmospheric adsorption features (McConnochie et al., 2013) may also be useful in this regard.

6.2.3. Calibration and analysis improvements

As calibration target surfaces get coated with airfall dust, the contrast between brighter and darker calibration targets is

reduced. This reduction in contrast may be used to quantify the optical thickness of dust layers. Such an approach has been employed for analysis of data from the MER Pancam (Kinch et al., 2007) and MSL Mastcam (Kinch et al., 2013) calibration targets. In both cases this dust-correction resulted in improved reflectance calibration of camera data. A similar approach can be employed on the ChemCam caltarget data. Furthermore, the calibration efforts would be strengthened by laboratory efforts to better characterize the photometric function of the Target #11 surface. Initial limited measurements conducted prior to the mission suggest that the surface is significantly non-Lambertian, an observation supported by in situ measurements on Mars. By combining this information with dust-coating mitigation efforts, calibration target observations other than the Sol 76 measurement could be considered for use. This would help reduce any residual uncertainties in spectral features that might result from variations in atmospheric opacity.

Mixture modeling analyses such as those conducted by Johnson et al. (2007) on Pancam spectra from the Spirit rover could better constrain the presence of minerals contributing to the ChemCam relative reflectance spectra. However, initial modeling efforts suggested that the limited wavelength coverage results in models that can be fitted equally well with a variety of mineral endmembers. Further efforts to refine mixing model techniques are therefore warranted.

6.2.4. Future observations

As the Curiosity rover continues its trek toward the entrance to Mt. Sharp, it will continue to sample targets with ChemCam LIBS for elemental analyses. Passive "dark" spectra will be acquired as a matter of course with these measurements, and dedicated passive observations may be made of particular targets of interest (e.g., additional vein materials, conglomerates, ejecta blocks). For example, ChemCam spectra of the spectrally distinct, hematite-bearing ridge discussed by Fraeman et al. (2013) may provide additional information on the spatial and spectral nature of hematite deposits. Measurements of the low-albedo dune field guarding the northwestern edge of Mt. Sharp will provide spectral information on another endmember unit in Gale crater. Materials excavated by the rover wheels may reveal hints of subsurface compositional variability as was found with Spirit on Husband Hill and surrounding Home Plate (Arvidson et al., 2006, 2008). Ultimately, long-distance and in situ ChemCam passive observations of the hematite-, sulfate- and phyllosilicate-rich terrains mapped from orbit (e.g., Milliken et al., 2010; Fraeman et al., 2013) will be useful documenting the visible/near-infrared spectral properties of the materials encountered and in guiding the rover traverse through these fascinating terrains.

Acknowledgments

The authors wish to thank the entire engineering and science teams who were integral in landing the Curiosity rover successfully, and in operating a complicated science instrument package efficiently to maximize the science return. In particular, the diligence of the downlink and uplink teams is truly appreciated, as is the generosity of the ChemCam team in agreeing to use the instrument in a manner distinct from its main purpose. The results demonstrated the excellent sensitivity of the instrument's spectrometers and the benefits of flexibility when operating instruments on Mars. K. Seelos (JHU/APL) provided the CRISM spectrum, and A. Ody (Université Paris-Sud, Orsay, France) provided the bright and dark OMEGA spectra. S. Clegg (LANL) provided the list of ChemCam targets assigned to specific geologic units. Helpful reviews were provided by M. Lane and an anonymous reviewer. J.R. Johnson was funded by the Mars Science Laboratory Participating Scientist program. The French contribution to MSL is supported by the Centre National d'Etudes Spatiales (CNES). Work by K. Kinch was supported by the Danish Council for Independent Research/Natural Sciences (FNU Grant 12-127126).

References

Anderson, R., Bridges, J., Williams, A., Edgar, L., Ollila, A., Williams, J., Nachon, M., Mangold, N., Dromart, G., Le Mouélic, S., Forni, O., Lanza, N., Wiens, R., Gupta, S., Blaney, D., Clark, B., Clegg, S., Gasnault, O., Lasue, J., Leveille, R., Lewin, E., Lewis, K.W., Maurice, S., Newsom, H., Sautter, V., Vaniman, D., 2015. ChemCam results from the Shaler outcrop in Gale crater, Mars. Icarus 249, 2–21.

Arvidson, R.E. et al., 2006. Overview of the Spirit Mars Exploration Rover mission to Gusev crater: Landing site to the Backstay outcrop in the Columbia Hills. J. Geophys. Res. 111, E02S01. http://dx.doi.org/10.1029/2005JE002499.

Arvidson, R.E. et al., 2008. Spirit Mars Rover Mission to the Columbia Hills, Gusev crater: Mission overview and selected results from the Cumberland Ridge to Home Plate. J. Geophys. Res. 113 (E12), E12S33.

Bell III, J.F., Ansty, T.M., 2007. High spectral resolution UV to near-IR observations of Mars using HST/STIS. Icarus 191, 581–602.

Bell III, J.F. et al., 2000. Mineralogic and compositional properties of martian soil and dust: Preliminary results from Mars Pathfinder. J. Geophys. Res. 105, 1721–1755.

Bell III, J.F. et al., 2003. The Mars Exploration Rover Athena Panoramic Camera (Pancam) investigation. J. Geophys. Res. 108 (E12). http://dx.doi.org/10.1029/2003JE002070.

Bell III, J.F. et al., 2004a. Pancam multispectral imaging results from the Spirit rover at Gusev crater. Science 305, 800–806.

Bell III, J.F. et al., 2004b. Pancam multispectral imaging results from the Opportunity rover at Meridiani Planum. Science 306, 1703–1709.

Bell III, J.F. et al., 2008. Visible to near-IR multispectral orbital observations of Mars. In: The Martian Surface: Composition, Mineralogy, and Physical Properties. Cambridge University Press, pp. 169–192 (Chapter 8).

Bell III, J.F. et al., 2013. Initial multispectral imaging results from the Mars Science Laboratory Mastcam investigation at the Gale crater field site. Lunar Planet. Sci. 44. Abstract #1417.

Bertelsen, P. et al., 2004. Report magnetic properties experiments on the Mars Exploration Rover Spirit at Gusev crater. Science 305 (5685), 827–829.

Bibring, J.-P. et al., 2004. OMEGA: Observatoire pour la Minéralogie, l'Eau, les Glaces et l'Activité. ESA SP 1240, pp. 37–49.

Bish, D.L. et al., 2013. X-ray diffraction results from Mars Science Laboratory: Mineralogy of Rocknest at Gale crater. Science 341 (6153). http://dx.doi.org/10.1126/science.1238932.

Blake, D.F. et al., 2013. Curiosity at Gale crater, Mars: Characterization and analysis of the Rocknest sand shadow. Science 341 (6153). http://dx.doi.org/10.1126/science.1239505.

Buz, J., Ehlmann, B.L., 2013. Bedrock composition and surface mineralogy of the greater gale region. Lunar Planet. Sci. 44. Abstract #2549.

Clancy, R.T., Wolff, M.J., Malin, M.C., 2006. MARCI ultraviolet global imaging of mars ozone and clouds. American Geophysical Union (Fall), vol. 1 (Abstracts).

Clark, R.N. et al., 2007, USGS Digital Spectral Library splib06a. U.S. Geological Survey, Data Series 231.

Cloutis, E.A., 2002. Pyroxene reflectance spectra: Minor absorption bands and effects of elemental substitutions. J. Geophys. Res. 107, 5039. http://dx.doi.org/10.1029/2001JE001590.

Cloutis, E.A. et al., 2006a. Detection and discrimination of sulfate minerals using reflectance spectroscopy. Icarus 184, 121–157.

Cloutis, E., Craig, M., Kaletzke, L., McCormack, K., Stewart, L., 2006b. HOSERLab: A new planetary spectrophotometer facility. Lunar Planet. Sci. 37. Abstract #2121.

Cloutis, E.A., McCormack, K.A., Bell III, J.F., Hendrix, A.R., Bailey, D.T., Craig, M.A., Mertzman, S.A., Robinson, M.S., Riner, M.A., 2008a. Ultraviolet spectral reflectance properties of common planetary minerals. Icarus 197, 321–347.

Cloutis, E.S., Craig, M.A., Kruzeleck, R.V., Jamroz, W.R., Scott, A., Hawthorne, F.C., Mertzman, S.A., 2008b. Spectral reflectance properties of minerals exposed to simulated Mars surface conditions. Icarus 195, 140–169.

Cloutis, E.A. et al., 2010. The 506 nm absorption feature in pyroxene spectra: Nature and implications for spectroscopy-based studies of pyroxene-bearing targets. Icarus 207, 295–313.

Drube, L. et al., 2010. Magnetic and optical properties of airborne dust and settling rates of dust at the Phoenix landing site. J. Geophys. Res. 115. http://dx.doi.org/10.1029/j009JE003419.

Fabre, C. et al., 2011. Onboard calibration igneous targets for the Mars Science Laboratory Curiosity rover and the Chemistry Camera laser induced breakdown spectroscopy instrument. Spectrochim. Acta B: Atom. Spectrosc. 66 (3–4), 280–289.

Farrand, W., Bell III, J.F., Johnson, J.R., Squyres, S.W., Soderblom, J., Ming, D.W., 2006. Spectral variability in visible and near infrared multispectral Pancam data collected at Gusev crater: Examinations using spectral mixture analysis and related techniques. J. Geophys. Res. 111, E02S15. http://dx.doi.org/10.1029/2005JE002495.

Farrand, W.H. et al., 2007. Visible and near-infrared multispectral analysis of rocks at Meridiani Planum, Mars, by the Mars Exploration Rover Opportunity. J. Geophys. Res. 112, E06S02. http://dx.doi.org/10.1029/2006JE002773.

Farrand, W.H. et al., 2008a. Rock spectral classes observed by the Spirit rover's Pancam on the Gusev crater plains and in the Columbia Hills. J. Geophys. Res. 113, E12S38. http://dx.doi.org/10.1029/2008JE003237.
Farrand, W.H., Bell III, J.F., Johnson, J.R., Bishop, J.L., Morris, R.V., 2008b. Multispectral imaging from Mars Pathfinder. In: The Martian Surface: Composition, Mineralogy, and Physical Properties. Cambridge University Press (Chapter 8).
Fraeman, A. et al., 2013. A hematite-bearing layer in Gale crater, Mars: Mapping and implications for past aqueous conditions. Geology 41, 1103–1106. http://dx.doi.org/10.1130/G43613.1.
Goetz, W. et al., 2005. Indication of drier periods on Mars from the chemistry and mineralogy of atmospheric dust. Nature 436 (7047), 62–65.
Goetz, W., Hviid, S.F., Kinch, K.M., Madsen, M.B., 2008. Magnetic properties of martian surface materials. In: The Martian Surface – Composition, Mineralogy, and Physical Properties, pp. 366.
Gondet, B., Audouard, J., Bibring, J.-P., Langevin, Y., 2013. OMEGA/Mars Express observations of Gale crater. Lunar Planet. Sci. 43. Abstract #2175.
Graff, T.G. et al., 2011. Dust removal on Mars using laser-induced breakdown spectroscopy. Lunar Planet. Sci. 42. Abstract 1916.
Greenberger, R.N., Mustard, J.F., Cloutis, E.A., Mann, P., Turner, K., 2013. Iron oxidation state in serpentines from visible imaging spectroscopy: Implications for planetary exploration and assessment of astrobiological potential. Lunar Planet. Sci. 44. Abstract #1296.
Grotzinger, J.P. et al., 2013. A habitable fluvio-lacustrine environment at Yellowknife Bay, Gale crater, Mars. Science. http://dx.doi.org/10.1126/science.1242777.
Hviid, S.F. et al., 1997. Report magnetic properties experiments on the Mars Pathfinder lander: Preliminary results. Science 278 (5344), 1768–1770.
Johnson, J.R., Grundy, W.M., 2001. Visible/near-infrared spectra and two-layer modeling of palagonite-coated basalts. Geophys. Res. Lett. 28, 2101–2104.
Johnson, J.R. et al., 2001. Geological characterization of remote field sites using visible and infrared spectroscopy: Results from the 1999 Marsokhod field test. J. Geophys. Res. 106, 7683–7711.
Johnson, J.R., Grundy, W.M., Lemmon, M.T., 2003. Dust deposition at the Mars Pathfinder landing site: Observations and modeling of visible/near-infrared spectra. Icarus 163, 330–346.
Johnson, J.R. et al., 2006. Radiative transfer modeling of dust-coated Pancam calibration target materials: Laboratory visible/near-infrared spectrogoniometry. J. Geophys. Res. 111, E12S07. http://dx.doi.org/10.1029/2005JE002658.
Johnson, J.R. et al., 2007. Mineralogic constraints on sulfur-rich soils from Pancam spectra at Gusev crater, Mars. Geophys. Res. Lett. 34, L13202. http://dx.doi.org/10.1029/2007GL029894.
Kinch, K.M., Sohl-Dickstein, J., Bell III, J.F., Johnson, J.R., Goetz, W., Landis, G.A., 2007. Dust deposition on the Mars Exploration Rover Panoramic Camera (Pancam) calibration targets. J. Geophys. Res. 112, E06S03. http://dx.doi.org/10.1029/2006JE002807.
Kinch, K.M., Madsen, M.B., Bell III, J.F., Johnson, J.R., Goetz, W., and the MSL Science Team, 2103. Dust on the Curiosity mast camera calibration target. Lunar Planet. Sci. 44. Abstract #1061.
Klima, R.L., Pieters, C.M., Dyar, M.D., 2007. Spectroscopy of synthetic Mg–Fe pyroxenes. I: Spin-allowed and spin-forbidden crystal field bands in the visible and near-infrared. Meteorit. Planet. Sci. 42, 235–253.
Lane, M.D., Bishop, J.L., Dyar, M.D., King, P.L., Parente, M., Hyde, B.C., 2008. Mineralogy of the Paso Robles soils on Mars. Am. Miner. 83 (5–6), 728–739.
Le Mouélic, S. et al., 2015. The ChemCam remote micro-imager at gale: Review of the first year on Mars. Icarus 249, 93–107.
Lemmon, M.T. et al., 2004. Atmospheric imaging results from the Mars Exploration Rovers: Spirit and Opportunity. Science 306, 1753–1756.
Léveillé, R.J. et al., 2014. Chemistry of fracture-filling raised ridges in Yellowknife Bay, Gale crater: Window into past aqueous activity and habitability on Mars. J. Geophys. Res., submitted for publication.
Madsen, M.B. et al., 2009. Overview of the magnetic properties experiments on the Mars Exploration Rovers. J. Geophys. Res. 114, E06S90. http://dx.doi.org/10.1029/2008JE003098.
Maurice, S. et al., 2012. The ChemCam instrument suite on the Mars Science Laboratory (MSL) rover: Science objectives and mast unit description. Space Sci. Rev. 170, 95–106.
McConnochie, T.H. et al., 2013. ChemCam passive spectroscopy of the martian atmosphere. American Geophysical Union (Fall) (Abstract).
McLennan, S.M. et al., 2013. Elemental geochemistry of sedimentary rocks at Yellowknife Bay, Gale crater, Mars. Science. http://dx.doi.org/10.1126/science.1244734.
McSween Jr., H.Y. et al., 1999. Chemical, multispectral, and textural constraints on the composition and origin of rocks at the Mars Pathfinder landing site. J. Geophys. Res. 104, 8679–8715.
Meslin, P.-Y. et al., 2013. Soil diversity and hydration as observed by ChemCam at Gale crater, Mars. Science 341 (6153). http://dx.doi.org/10.1126/science.1238670.
Milliken, R.E., Grotzinger, J.P., Thomson, B.J., 2010. Paleoclimate of Mars as captured by the stratigraphic record in Gale crater. Geophys. Res. Lett. 37, 4. http://dx.doi.org/10.1029/2009GL041870.
Milton, E.J. et al., 2009. Progress in field spectroscopy. Rem. Sens. Environ. 113, S92–S109.
Ming, D.W. et al., 2013. Volatile and organic compositions of sedimentary rocks in Yellowknife Bay, Gale crater, Mars. Science. http://dx.doi.org/10.1126/science.1245267.
Morris, R.V., Lauer Jr., H.V., Lawson, C.A., Gibson Jr., E.K., Nace, G.A., Stewart, C., 1985. Spectral and other physicochemical properties of submicron powders of hematite (α-Fe_2O_3), maghemite (γ-Fe_2O_3), magnetite (Fe_3O_4), goethite (α-FeOOH), and lepidocrocite (γ-FeOOH). J. Geophys. Res. 90, 3126–3144.
Morris, R.V., Golden, D.C., Bell III, J.F., 1997. Low-temperature reflectivity spectra of red hematite and the color of Mars. J. Geophys. Res. 102, 912–9133.
Nachon, M. et al., 2014. Calcium sulfate characterized by ChemCam/Curiosity at Gale crater, Mars. Lunar Planet. Sci. XLV. Abstract #2006.
Nachon, M. et al., 2013. Calcium sulfate veins characterized by the ChemCam instrument at Gale crater, Mars. Geochim. Cosmochim. Acta, submitted for publication.
Ody, A. et al., 2012. Global maps of anhydrous minerals at the surface of Mars, from OMEGA/MEx. J. Geophys. Res.. http://dx.doi.org/10.1029/2012JE004117.
Roush, T.L., Blaney, D.L., Singer, R.B., 1993. The surface composition of Mars as inferred from spectroscopic observations. In: Pieters, C.M., Englert, P.A.J. (Eds.), Remote Geochemical Analysis: Elemental and Mineralogical Composition. Cambridge University Press, New York, pp. 367–393.
Singer, R.B., McCord, T.B., Clark, R.N., Adams, J.B., Huguenin, R.L., 1979. Mars surface composition from reflectance spectroscopy: A summary. J. Geophys. Res. 84, 8415–8426.
Stack, Kathryn M., MSL Science Team, 2013. An overview of past depositional environments explored by the Curiosity rover at Bradbury landing and Yellowknife Bay, Gale crater, Mars. In: Geological Society of America Abstracts with Programs, vol. 45, no. 7.
Vaniman, D. et al., 2012. Ceramic ChemCam calibration targets on Mars Science Laboratory. Space Sci. Rev. 170 (1–4), 229–255.
Vaniman, D.T. et al., 2013. Mineralogy of a mudstone at Yellowknife Bay, Gale crater, Mars. Science. http://dx.doi.org/10.1126/science.1243480.
Vasavada, A.R. et al., 2013. Mars Science Laboratory: First 100 sols monitoring the atmosphere and environment within Gale crater. Lunar Planet Sci. 44. Abstract #1191.
Vaughan, A.F. et al., 2010. Pancam and Microscopic Imager observations of dust on the Spirit rover: Cleaning events, spectral properties, and aggregates. Mars 5, 129–145. http://dx.doi.org/10.1555/mars.2010.0005.
Wiens, R. et al., 2012. The ChemCam instrument suite on the Mars Science Laboratory (MSL) rover: Body unit and combined system performance. Space Sci. Rev. 170, 167–227.